

1 **HiTIC-Monthly: A Monthly High Spatial Resolution (1**
2 **km) Human Thermal Index Collection over China during**
3 **2003–2020**

4
5 Hui Zhang¹, Ming Luo^{1,3*}, Yongquan Zhao^{2*}, Lijie Lin⁴, Erjia Ge⁵, Yuanjian Yang⁶,
6 Guicai Ning³, Jing Cong⁷, Zhaoliang Zeng⁸, Ke Gui⁹, Jing Li¹⁰, Ting On Chan¹, Xiang
7 Li¹, Sijia Wu¹, Peng Wang¹, Xiaoyu Wang¹

8
9 ¹School of Geography and Planning, and Guangdong Key Laboratory for Urbanization and Geo-
10 simulation, Sun Yat-sen University, Guangzhou 510006, China.

11 ²School of Geospatial Engineering and Science, Sun Yat-sen University, and Southern Marine Science
12 and Engineering Guangdong Laboratory (Zhuhai), Zhuhai 519082, China.

13 ³Institute of Environment, Energy and Sustainability, The Chinese University of Hong Kong, Hong Kong
14 SAR, China.

15 ⁴School of Management, Guangdong University of Technology, Guangzhou 510520, China.

16 ⁵Dalla Lana School of Public Health, University of Toronto, Toronto, Ontario M5T 3M7, Canada.

17 ⁶School of Atmospheric Physics, Nanjing University of Information Science & Technology, Nanjing
18 210044, China.

19 ⁷Tianjin Municipal Meteorological Observatory, Tianjin 300074, China.

20 ⁸State Key Laboratory of Severe Weather, Chinese Academy of Meteorological Sciences, Beijing
21 100081, China.

22 ⁹State Key Laboratory of Severe Weather (LASW) and Key Laboratory of Atmospheric Chemistry
23 (LAC), Chinese Academy of Meteorological Sciences, Beijing 100081, China.

24 ¹⁰College of Resources and Environment, Fujian Agriculture and Forest University, Fuzhou 35002,
25 China.

26
27 **Correspondence to:* Ming Luo (luom38@mail.sysu.edu.cn) and Yongquan Zhao
28 (zhaoyq66@mail.sysu.edu.cn)

30 **Abstract**

31 Human-perceived thermal comfort (also known as human-perceived temperature) measures the
32 combined effects of multiple meteorological factors (e.g., temperature, humidity, and wind speed) and
33 can be aggravated under the influences of global warming and local human activities. With the most
34 rapid urbanization and the largest population, China is being severely threatened by aggravating human
35 thermal stress. However, the variations of thermal stress in China at a fine scale have not been fully
36 understood. This gap is mainly due to the lack of a high-resolution gridded dataset of human thermal
37 indices. Here, we generated the first high spatial resolution (1 km) dataset of monthly human thermal
38 index collection (HiTIC-Monthly) over China during 2003–2020. In this collection, 12 commonly-used
39 thermal indices were generated by the **Light Gradient Boosting Machine (LGBM)** learning algorithm
40 from multi-source data, including land surface temperature, topography, land cover, population density,
41 and impervious surface fraction. Their accuracies were comprehensively assessed based on the
42 observations at 2419 weather stations across the mainland of China. The results show that our dataset
43 has desirable accuracies, with the mean R^2 , root mean square error, and mean absolute error of 0.996,
44 0.693°C, and 0.512°C, respectively, by averaging the 12 indices. Moreover, the data exhibit high
45 agreements with the observations across spatial and temporal dimensions, demonstrating the broad
46 applicability of our dataset. A comparison with two existing datasets also suggests that our high-
47 resolution dataset can describe a more explicit spatial distribution of the thermal information, showing
48 great potentials in fine-scale (e.g., intra-urban) studies. Further investigation reveals that nearly all
49 thermal indices exhibit increasing trends in most parts of China during 2003–2020. The increase is
50 especially significant in North China, Southwest China, the Tibetan Plateau, and parts of Northwest
51 China, during spring and summer. The HiTIC-Monthly dataset is publicly available via
52 <https://zenodo.org/record/6895533> (Zhang et al., 2022a).

53

54 **1 Introduction**

55 Global climate change has brought significant challenges to human society and natural systems (Arias et
56 al., 2021; Haines and Ebi, 2019) by inducing higher air temperature and more frequent extreme weather
57 and climate events around the world (Arias et al., 2021; Schwingshackl et al., 2021). Heat-related
58 disasters, e.g., heatwaves, droughts, and wildfires, are occurring more frequently and becoming more
59 intense (Tong et al., 2021; Arias et al., 2021; Luo et al., 2022), exacerbating the thermal environment
60 and threatening the tolerance limits of humans, animals, and plants (Raymond et al., 2020). Substantial
61 warming and increasing extreme weather and climate events aggravate human thermal comfort and
62 increase the exposures to uncomfortable thermal environments (Brimicombe et al., 2021), thus posing
63 adverse impacts on public health, socio-economy, and agricultural productivities (Budhathoki and
64 Zander, 2019; Moda et al., 2019; Tuholske et al., 2021; Sun et al., 2019; Zhao et al., 2017).

65
66 The thermal stress that human beings actually perceive is not only related to air temperature, but also
67 jointly influenced by other environmental variables such as humidity, wind, and/or direct sunlight (Mistry,
68 2020; Djongyang et al., 2010). These variables alter the heat balance that maintains the core temperature
69 of human bodies by influencing the heat exchange (e.g., radiation, convection, conduction, and
70 evaporation) between humans and the surrounding environment (Periard et al., 2021; Stolwijk, 1975).
71 High atmospheric humidity can exacerbate the thermal stress on human bodies by reducing evaporation
72 from the skin through sweating when the air temperature is high (Li et al., 2018; Rogers et al., 2021; Luo
73 and Lau, 2021). Furthermore, abnormal weather with a combination of extremely high air temperature,
74 humidity, and/or wind can reduce labor capacity and human performance (Roghanchi and Kocsis, 2018;
75 Lazaro and Momayez, 2020; Enander and Hygge, 1990), leading to temperature-related discomfort,
76 stress, morbidity, and even death (Di Napoli et al., 2018; Kuchcik, 2021; Nastos and Matzarakis, 2011),
77 particularly during heatwaves. For example, in the summer of 2017, 2018, and 2019, there were 1489,
78 1700, and 161 heatwave-related deaths, respectively, in the United Kingdom (Rustemeyer and Howells,
79 2021). Additionally, vulnerable groups including children, the elderly, chronic patients, and poor
80 communities are at higher risk of being affected by thermal stress (Patz et al., 2005; Wang et al., 2019),
81 which is likely to be further exacerbated as global population aging and climate warming (United Nations,
82 2017).

83

84 The changes and impacts of human thermal stress have attracted increasing attention in recent years
85 (Schwingshackl et al., 2021; Krzysztof et al., 2021; Li et al., 2018; Rahman et al., 2022; Ren et al., 2022;
86 Luo and Lau, 2021). For instance, Szer et al. (2022) estimated the impact of heat stress on construction
87 workers based on the Universal Thermal Climate Index (UTCI). Ren et al. (2022) and Luo and Lau (2021)
88 quantified the contribution of urbanization and climate change to urban human thermal comfort in China.
89 Schwingshackl et al. (2021) assessed future severity and trend of global heat stress based on Coupled
90 Model Intercomparison Project phase 6 (CMIP6). These studies were mainly based on meteorological
91 stations or coarse-gridded data. However, the meteorological stations are sparsely distributed (Peng et
92 al., 2019), particularly in undeveloped and mountainous areas, which cannot reveal continuously spatial
93 distributions of air temperature and thermal stress conditions (He et al., 2021). Additionally, existing low
94 spatial resolution image products (Mistry, 2020; Di Napoli et al., 2020) cannot be applied to fine-scale
95 studies because they cannot provide information with spatial details and variations. However, the changes
96 of human thermal stress at a fine scale (e.g., 1 km×1 km) remain much less understood. This research
97 gap is mainly inhabited by the unavailability of a high spatial resolution (high-resolution) gridded dataset
98 of human thermal stress.

99

100 Although extensive studies have been conducted to generate high-resolution land surface temperature
101 (LST) [such as the Land Surface Temperature in China (LSTC; (Zhao et al., 2020) and the global
102 seamless land surface temperature dataset (Zhang et al., 2022b; Hong et al., 2022)], or near surface air
103 temperatures (SAT) products [such as ERA5 (ECMWF, 2017), TerraClimate (Abatzoglou et al., 2018),
104 and GPRChinaTemp1km (He et al., 2021)], human thermal stress datasets were generally produced at
105 low-resolution levels, such as ERA5-HEAT (Di Napoli et al., 2020), HDI_0p25_1970_2018 (hereafter,
106 HDI) (Mistry, 2020), and HiTiSEA (Yan et al., 2021). ERA5-HEAT was derived from ERA5, and
107 includes two global hourly human thermal stress indices (UTCI and mean radiant temperature (MRT))
108 from January 1979 to the present (Di Napoli et al., 2020). The HDI dataset was generated using 3-hourly
109 climate variables of the global land data assimilation system (GLDAS), and it contains ten daily indices
110 with a spatial resolution of $0.25^{\circ} \times 0.25^{\circ}$, covering 90°N – 60°S from 1970 to 2018 (Mistry, 2020).
111 HiTiSEA contains ten daily human thermal stress indices from 1981 to 2017, with a spatial resolution of

112 $0.1^\circ \times 0.1^\circ$ over South and East Asia (Yan et al., 2021), which was derived from the ERA5-Land and
113 ERA5 reanalysis products. However, these existing thermal index datasets have very coarse spatial
114 resolutions. There is an urgent need for a high-resolution (e.g., 1 km) data collection of multiple human
115 thermal stress indices.

116

117 Various indices have been proposed to measure human thermal stress, but there is no universal thermal
118 stress index that works in all climate zones (Schwingshackl et al., 2021; Brake and Bates, 2002;
119 Roghanchi and Kocsis, 2018; Luo and Lau, 2021). Existing human thermal stress indices considered
120 different climate conditions, direct or indirect exposures to weather elements, human metabolism, and
121 the local working environment (Di Napoli et al., 2020), which were designed to evaluate or quantify the
122 comprehensive environmental pressure of meteorological factors (e.g., temperature, humidity, wind) on
123 human bodies (Epstein and Moran, 2006). These indices are based on the thermal exchange between the
124 human and surrounding environments or empirical relationships gained by studying human responses to
125 various environmental factors, varying in complexity, applicability, and capacity (Staiger et al., 2019).
126 For example, the heat index (HI) is used for meteorological service (NWS, 2011); wet-bulb temperature
127 (WBT) is used to measure the upper physiological limit of human beings (Raymond et al., 2020);
128 physiologically equivalent temperature (PET) and UTCI are used to estimate human thermal comfort
129 (Varentsov et al., 2020). Therefore, a high-resolution dataset that contains different commonly used
130 human thermal stress indices is urgently called in global and regional studies, particularly for those with
131 complex climate conditions (e.g., China).

132

133 China has been threatened by deteriorating thermal environments under global climate change and rapid
134 local urbanization over the past decades (Ren et al., 2022; Luo and Lau, 2019). The changes and
135 characteristics of human thermal stress across China have attracted extensive attention in recent years
136 (Yan, 2013; Tian et al., 2022; Li et al., 2022). Wang et al. (2021) found that the frequency of extreme
137 human-perceived temperature events increases in summer and decreases in winter in most urban
138 agglomerations (UAs) of China. Li et al. (2022) showed that the frequency of thermal discomfort days
139 in China exhibits a significant increasing trend from 1961 to 2014, and there will be more threats from
140 thermal discomfort in the future. Therefore, a long-term and high-resolution dataset with multiple human

141 thermal stress indices in China is of great importance for investigating detailed spatial and temporal
142 variations of human thermal stress across the country. Such a dataset has the potential to (1) assess
143 population exposure to extreme thermal conditions and heat-related health risks, (2) reveal the
144 spatiotemporal evolution of human thermal stress and its influence on public health, tourism, industries,
145 military, epidemiology, and biometeorology at a fine scale, and (3) provide policymakers with data in
146 manipulating targeted strategies to mitigate heat stress and protect vulnerable people.

147

148 In this study, we produced a high-resolution ($1 \text{ km} \times 1 \text{ km}$) thermal index collection at a monthly scale
149 (HiTIC-Monthly) in China over a long period (2003–2020). This collection contains 12 widely-used
150 human thermal indices, including Surface Air Temperature (SAT), indoor Apparent Temperature (AT_{in}),
151 outdoor shaded Apparent Temperature (AT_{out}), Discomfort Index (DI), Effective Temperature (ET), Heat
152 Index (HI), Humidex (HMI), Modified Discomfort Index (MDI), Net Effective Temperature (NET),
153 Wet-Bulb Temperature (WBT), simplified Wet Bulb Globe Temperature (sWBGT), and Wind Chill
154 Temperature (WCT). The remainder of this paper is structured as follows. Sections 2 and 3 describe the
155 data sources and the methodology, respectively. Section 4 presents a comprehensive analysis of the
156 accuracies and trends of the human thermal indices. Comparisons on our products with two existing
157 datasets are in Section 5, data availability is provided in Section 6. The main findings of this paper are
158 summarized in Section 7.

159

160 **2 Data**

161 **2.1 Meteorological data**

162 Daily mean surface air temperature, relative humidity, and wind speed recorded at the 2419 weather
163 stations across China (Figure 1) during 2003–2020 were collected from the China Meteorological Data
164 Service Center (CMDC) at <http://data.cma.cn/en>. All station records were subjected to strict quality
165 control and evaluation, including homogenization based on a statistical approach (Xu et al., 2013) and
166 evaluation of temporal inhomogeneity based on the Easterling-Peterson method (Li et al., 2004).

167 2.2 Covariates

168 Human thermal stress is related to temperature, topography, land cover, population density, surface water,
169 and vegetation (Wang et al., 2020; Rahman et al., 2022; Krzysztof et al., 2021). In this study, eight
170 variables reflecting the changes and spatial distribution characteristics of temperature were used to
171 predict human thermal indices (Table 1) in addition to the meteorological variables. As LST is one of the
172 most essential parameters for predicting human thermal indices, the seamless LST dataset created by
173 Zhang et al. (2022b) was introduced into our model training. This LST dataset used a spatiotemporal
174 gap-filling algorithm to fill the missing or invalid value caused by clouds in the Moderate Resolution
175 Imaging Spectroradiometer (MODIS) LST dataset (MOD11A1 and MYD11A1). It includes daily mid-
176 daytime (13:30) and mid-nighttime (01:30) LST with 1 km spatial resolution. The mean root mean
177 squared errors (*RMSEs*) of daytime and nighttime LST are 1.88°C and 1.33°C, respectively. We used
178 monthly LST as one of the inputs to predict the spatial distribution of 12 thermal indices. Monthly LST
179 values were calculated by averaging daily LST, which was obtained by averaging four observations in a
180 day, including mid-daytime and mid-nighttime observations from ascending and descending orbits of
181 MOD11A1 (Terra) and MYD11A1 (Aqua). More details about the LST data are described in Zhang et al.
182 (2022b). The land cover dataset (MCD12Q1 Version 6) developed by Sulla-Menashe and Friedl (2019)
183 based on a supervised classification method was downloaded via Google Earth Engine (GEE). The Multi-
184 Error-Removed Improved-Terrain (MERIT) elevation dataset developed by Yamazaki et al. (2017) was
185 downloaded from GEE. This dataset was generated after removing the errors from existing Digital
186 Elevation Models (DEMs), such as SRTM3 and AW3D-30m, based on multi-source satellite data and
187 filtering algorithms. The spatial resolution of this dataset is 3" (i.e., ~90 meters at the equator). In addition,
188 the slope was also extracted from the elevation data to act as the topography predictor. As the artificial
189 surface is closely related to human activities (Zhao and Zhu, 2022), the dataset of global artificial
190 impervious area (GAIA) produced by Gong et al. (2020) from the Google Earth Engine (GEE) was used
191 to delineate human footprints. The overall accuracy of GAIA is greater than 90% (Gong et al., 2020).
192 The population dataset was downloaded from the WorldPop Project (Gaughan et al., 2013). Then, the
193 abovementioned eight datasets were pre-processed to have the same spatial extend, projection, and spatial
194 resolution (1 km) through image mosaicking, reprojection, resampling, clipping, aggregating, and
195 monthly synthesizing. Moreover, year and month of the year were also used as covariates. Note that we

196 did not include precipitation as a covariate because the precipitation data are not normally distributed.
197 More importantly, they exhibit many zero values in many regions of China (especially in the dry season),
198 which would increase the uncertainty of the spatial prediction.

199

200 **3 Methodology**

201 **3.1 Calculation of human thermal indices**

202 In addition to SAT, the calculation of human thermal indices used in this study is described in Table 2.
203 These indices are first calculated based on SAT (also simply denoted as T), relative humidity (RH), wind
204 speed (V), and actual vapor pressure (E_a) at daily scale. E_a is derived from T and RH rather than directly
205 observed at meteorological stations (Eqs. 1~2; (Bolton, 1980)). Furthermore, monthly human thermal
206 indices were derived by averaging daily values in each month.

$$207 \quad E_s = 6.112 \times \exp^{(17.67 \times T / (T + 243.5))} \quad (1)$$

$$208 \quad E_a = \frac{RH}{100} \times E_s \quad (2)$$

209 Here E_s is saturation vapor pressure (hPa) near the surface, T (°C) is air temperature at 2 m above the
210 ground, and RH (%) is relative humidity at 2 m above the ground.

211

212 **3.2 Prediction of human thermal indices using LGBM**

213 The Light Gradient Boosting Machine (LGBM) algorithm was employed to predict human thermal
214 indices during 2003–2020. LGBM is one of the gradient boosting decision tree (GBDT) algorithms
215 developed by Microsoft Research (Ke et al., 2017). This algorithm has become a very popular nonlinear
216 machine learning algorithm due to its superior performance in machine learning competitions and
217 efficiency (Candido et al., 2021). Its performance has been evaluated and shows desirable results in
218 different applications, such as evapotranspiration estimation (Fan et al., 2019), land cover classification
219 (Candido et al., 2021; Mccarty et al., 2020), air quality prediction (Su, 2020; Zeng et al., 2021; Tian et
220 al., 2021), subsurface temperature reconstruction (Su et al., 2021), and above-ground biomass estimation
221 (Tamiminia et al., 2021).

222

223 Furthermore, LGBM adopts the Gradient-based One-Side Sampling (GOSS) and Exclusive Feature
 224 Bundling (EFB) algorithms to improve the training speed (Su et al., 2021). Here, GOSS is used to select
 225 data instances with larger gradients and to exclude a considerable proportion of small gradient data
 226 instances (Ke et al., 2017), and EFB is used to merge features (Ke et al., 2017). Compared with traditional
 227 GBDT algorithms including eXtreme gradient boosting (XGBoost) and Stochastic Gradient Boosting
 228 (SGB), LGBM effectively decreases the training time without reducing the accuracy (Los et al., 2021;
 229 Ke et al., 2017).

230

231 We used the Python package *Scikit-Learn* to perform the LGBM training, and hyperparameters of LGBM
 232 were tuned based on Grid Search Methods. The observed monthly human thermal indices at the 2419
 233 weather stations across the mainland of China during 2003–2020 were randomly classified into a training
 234 set (80%) for hyperparameters tuning and model training and a testing set (20%) for model evaluation.

235

236 3.3 Accuracy assessment

237 Four statistic metrics, namely, determination coefficient (R^2), Mean Absolute Error (MAE), $RMSE$, and
 238 $Bias$ (Rice, 2006), were used to evaluate the prediction accuracy of the human thermal indices. Ranging
 239 from 0 to 1, R^2 measures the proportion of variance explained by the model, representing how well the
 240 human thermal indices were predicted compared to the observations. MAE represents the average
 241 absolute error between the predictions and the observations. $RMSE$ is the standard deviation of the
 242 residuals and is sensitive to outliers. $Bias$ describes the differences between the predictions and the
 243 observations. These metrics are computed as follows.

$$244 \quad MAE = \frac{1}{N} \times \sum_{i=1}^N |y_i - \hat{y}| \quad (3)$$

$$245 \quad RMSE = \sqrt{\frac{1}{N} \times \sum_{i=1}^N (y_i - \hat{y})^2} \quad (4)$$

$$247 \quad R^2 = 1 - \frac{\sum_{i=1}^N (y_i - \hat{y})^2}{\sum_{i=1}^N (y_i - \bar{y})^2} \quad (5)$$

$$248 \quad Bias = \frac{1}{N} \times \sum_{i=1}^N (y_i - \hat{y}) \quad (6)$$

249 where \hat{y} is the predicted value of human thermal indices, \bar{y} is the mean of the observed human thermal

250 indices calculated from meteorological stations, and N is the number of samples.

251

252 **4 Results**

253 **4.1 Evaluation of the predicted human thermal indices**

254 **4.1.1 Overall accuracy**

255 The prediction accuracies of the 12 human thermal indices were evaluated based on the validation data
256 introduced in Section 3.2. All predicted human thermal indices exhibit high accuracies. Figure 2 shows
257 the scatter plots of the observed versus the predicted values of the 12 human thermal indices. As the
258 figure displays, the data points of all indices are concentrated around the corresponding 1:1 line,
259 indicating a good consistency between the observed and the predicted values. Figure 3 and Table 3
260 present the R^2 , MAE , $RMSE$, and $Bias$ values of 12 thermal indices during 2003–2020. The R^2 values of
261 the 12 indices are all higher than 0.99, and their $RMSE$, MAE , and $Bias$ are lower than 0.9 °C, 0.7 °C,
262 and 0.003 °C, respectively. Particularly, HMI has the largest $RMSE$ (0.859 °C) and MAE (0.645 °C),
263 while ET shows the smallest $RMSE$ (0.377 °C) and MAE (0.281 °C). The larger errors of NET are likely
264 caused by the incorporation of wind speed during the computation (see Table 2). Overall, the accuracy
265 metrics demonstrate that the 12 predicted human thermal indices are of good quality.

266

267 The spatial distributions of R^2 , MAE , $RMSE$, and $Bias$ at individual stations across the mainland of
268 China are depicted in Figures 4–7, respectively. The predicted indices have high R^2 values
269 (i.e., >0.98, Figure 4) at almost all stations across China, demonstrating the superiority of LGBM.
270 Better predictions (with higher R^2) are distributed in eastern China, particularly in the North China
271 Plain (NCP) and the Yangtze River Delta (YRD), while southwestern China (e.g., the Yunnan-
272 Guizhou Plateau (YGP)) has relatively lower R^2 values (<0.98). For MAE and $RMSE$, all indices
273 have small values <1 °C at most stations across China. HMI has the largest MAE and $RMSE$ values
274 (Figures 5g and 6g), followed by NET and WCT, and ET has the smallest MAE and $RMSE$ values
275 (i.e., < 0.4 °C, Figures 5e and 6e). The MAE and $RMSE$ of NET and WCT decrease from
276 northwestern to southeastern China (Figures 5i, 5l, 6i, 6l). For other indices, small MAE and $RMSE$
277 values are mainly observed in plains including NCP, while large values tend to appear in regions

278 with complex topography, such as arid Northwest China, mountainous Northeast and South China,
279 and the Hengduan Mountains. These differences are related to the uneven distribution of weather
280 stations, i.e., dense in plains and coarse in complex terrain areas. The *Bias* values range from -0.3°
281 C to $0.3^{\circ}C$ (Figure 7). Positive and negative *Bias* values are mainly distributed in northern and
282 southern China, respectively.

283

284 **4.1.2 Annual and monthly accuracies**

285 The annual accuracies regarding *RMSE*, *MAE*, and *Bias* of the 12 human thermal indices during 2003–
286 2020 are shown in Figure 8. *RMSEs* and *MAEs* of all indices in nearly all years are less than $1.0^{\circ}C$
287 (Figures 8a-b). Yearly *RMSE* (*MAE*) of ET fluctuates around $0.3^{\circ}C$ ($0.2^{\circ}C$) during 2003–2020. *RMSEs*
288 (*MAEs*) of other indices range from 0.5 to $1.1^{\circ}C$ (0.4 – $0.8^{\circ}C$) with marginal variations from year to year.
289 *Biases* vary between $-0.04^{\circ}C$ and $0.04^{\circ}C$ across all years. *Biases* seem to be slightly positive in 2003,
290 2004, and 2014 and negative in 2012, 2017, and 2018. Moreover, Figure S1 displays the monthly *RMSEs*,
291 *MAEs*, and *Biases* of all human thermal indices. For *RMSE*, all the indices in 12 months are lower than
292 $1.4^{\circ}C$, and their *MAEs* are less than $1^{\circ}C$. HI and HMI have relatively higher *RMSE* and *MAE* values in
293 summer than in other seasons; whereas, other indices tend to have larger errors in winter than in summer.
294 Additionally, the magnitude of *Bias* is smaller than $0.03^{\circ}C$ for all the indices in 12 months.

295

296 **4.1.3 Accuracies in major urban agglomerations**

297 More than half of the national population in China lives in cities, particularly in UAs (i.e., also known as
298 city clusters). Here we assessed the prediction accuracies in 20 major UAs in China, which hold 62.83%
299 and 80.57% of the total population and gross domestic product (GDP) of the country (Fang, 2016). These
300 accuracy assessments are presented in Tables S1–S4. As shown in Table S1, all UAs have the R^2 values
301 higher than 0.9837, with an average of 0.9947. Table S2 also shows that these UAs have small *RMSE*
302 values, most of which are smaller than $1^{\circ}C$, except for the UA of North Tianshan Mountain in arid
303 Northwest China. As the biggest UA in China, YRD has the lowest *RMSE* of $0.288^{\circ}C$ among all 20 UAs.
304 The *MAEs* of the thermal indices in all UAs are smaller than $1^{\circ}C$ and with an average value of $0.477^{\circ}C$
305 (Table S3). The *Biases* in the 20 UAs range from $-0.160^{\circ}C$ to $0.123^{\circ}C$ (Table S4). These results suggest

306 that all predicted human thermal indices in different UAs across China are of good quality at the local
307 scale. It implies that our prediction model and results have great potential in evaluating local thermal
308 environment changes (e.g., in urban areas or cities).

309

310 **4.2 Spatial variations of the human thermal indices**

311 The abovementioned assessments show that our model based on LGBM can yield high-accuracy
312 predictions at both national and local scales. Therefore, this model is employed to generate a high-
313 resolution human thermal index collection at a monthly scale over China (HiTIC-Monthly) during 2003–
314 2020. By taking monthly ET in 2020 as an example, we examined the monthly evolution of spatial
315 patterns of the HiTIC-Monthly dataset in this subsection.

316

317 Figure 9 shows the monthly distribution of the predicted ET in 2020, which exhibits obvious seasonality
318 with higher temperatures in summer and lower in winter. The temperature shows a significant zonal
319 difference with colder temperatures in northern than southern China. Temperature has a close relationship
320 with topography and decreases with elevation, varying from plateaus to plains. The Qinghai-Tibet Plateau
321 (TP) has the lowest temperature, while southern China, the Sichuan Basin, and the Gobi regions in
322 Northwest China witness the highest temperature. The distribution of temperature exhibits different
323 patterns among the four seasons, especially between winter (e.g., January) and summer (e.g., July). In
324 winter, the temperature increases from northern to southern areas and is the coldest in Northeast and
325 Northwest China and the warmest on the Hainan Island. In summer, the hottest temperature appears in
326 the Tarim and Jungar Basins of Xinjiang. The NCP region also has a high temperature in summer, which
327 might be related to local urbanization (Liu et al., 2008) and irrigation (Kang and Eltahir, 2018).

328

329 The spatial variations of the predicted human thermal indices in summer (which is often characterized
330 by severe heat stress) are examined in Figure 10 by taking July 2020 as an example. As it shows, the 12
331 indices exhibit similar distribution patterns. There are significant differences in temperature among
332 northwest, northeast, and southeast China. Generally, the temperature decreases from the southeast to the
333 northwest, and the southeast and northwest parts have the highest and lowest temperatures, respectively.

334

335 HMI exhibits the highest temperature while NET shows the lowest in July 2020. The dominant modes of
336 these indices are further examined by applying the empirical orthogonal function (EOF) analysis (Figures
337 S10–S13). As Figure S10 shows, the leading EOF (EOF1) of all 12 thermal indices exhibit highly
338 consistent spatial distribution with higher values in the northern region and lower values in the south.
339 Their temporal variations are also similar to each other (Figure S11). The second and third EOF modes
340 (EOF2 and EOF3) are also similar among different thermal indices (except EOF3 of NET, Figures S11–
341 S13). These results demonstrate the desirable quality of our products.

342

343 4.3 Temporal changes in the human thermal indices

344 The yearly evolutions of the annual mean human thermal indices during 2003–2020 are displayed in
345 Figure 11. Despite the interannual fluctuation in the time series, all indices exhibit upward trends except
346 for NET and WCT, of which the decreasing trends are mainly affected by the recovering wind speed in
347 the recent decade (Zeng et al., 2019). The fastest warming appears in HMI (0.303 °C/decade), and the
348 slowest is in ET (0.111 °C/decade). These warming trends are stronger than the rising rate of global mean
349 near surface temperature (IPCC, 2021), demonstrating China as one of the severest hotspots suffering
350 from dramatic climate warming under global change. The detailed spatial variations regarding the trends
351 of the human thermal indices across China are further depicted in Figure 12. Most parts of China
352 experience are seen with increases in nearly all the indices during 2003–2020. These increases are
353 especially more profound in North China, Southwest China, TP, and parts of Northwest China. The
354 possible reasons for the prominent warming trends in North China are explained as follows. The
355 urbanization process has been prevailing in this area, with rapid growth in the economy and population.
356 This process is accompanied by dramatic increases in impervious surfaces and decreases in green spaces.
357 These changes lead to warmer surface and near surface air temperature, known as urban heat islands
358 (UHI), thus increasing thermal stress in this region. The urbanization effects on local heat stress have
359 also been reported by (Luo and Lau, 2021). Moreover, North China has a large amount of croplands with
360 prominent irrigation activities, which may increase air humidity near the surface and exacerbate the
361 combined effects of temperature and humidity, leading to increased heat stress (Kang and Eltahir, 2018).
362 In addition, this area has experienced a weakening of surface wind speed (Zhang et al., 2021), which also
363 exacerbates thermal stress, especially in NET and WCT.

364

365 Furthermore, different indices have different degrees of increasing trends. HMI has the largest
366 increasing magnitude (Figure 12h), and ET is seen with relatively slight increases across China
367 (Figure 12f). The trends of NET and WCT have similar spatial distribution patterns, with large
368 proportions having cooling trends since 2003 (Figures 12j&l). Most parts of Xinjiang, northeastern
369 and southern China have obvious decreasing trends, and the Inner Mongolia Plateau (IMP), NCP,
370 eastern TP, YRD, and YGP have slight increasing trends.

371

372 The temporal trends of the human thermal indices in different seasons were also examined (Figure 13).
373 The fastest warming tendency is observed in the spring season. The rising trends of spring HMI, HI, MDI,
374 AT_{in} , and AT_{out} exceed $0.4\text{ }^{\circ}\text{C}/\text{decade}$, and the trends of other indices (except ET and NET) are larger
375 than $0.3\text{ }^{\circ}\text{C}/\text{decade}$ (Figure S2). Summer also has been experiencing significant increasing trends in all
376 indices, i.e., at a rate of $> 0.2\text{ }^{\circ}\text{C}/\text{decade}$ (except ET and NET). The trends in summer HMI, HI, WBT,
377 MDI, DI, sWBGT, AT_{in} , and AT_{out} exceed $0.3\text{ }^{\circ}\text{C}/\text{decade}$ (Figure S3). Differing from spring and summer,
378 the human thermal indices (except WCT and NET) in the autumn season show slightly cooling trends
379 (Figure S4). Autumn WCT and NET have significantly strong decreasing trends, i.e., -0.349 and $-$
380 $0.507\text{ }^{\circ}\text{C}/\text{decade}$, respectively. Similar strong cooling trends of WCT and NET appear in winter, i.e., $-$
381 0.661 and $-0.453\text{ }^{\circ}\text{C}/\text{decade}$, respectively, while other indices experience marginal long-term changes
382 (Figure S5).

383

384 Figure S6 maps the spatial patterns of the trends of summer mean human thermal indices over the
385 mainland of China during 2003–2020. All indices show warming trends in most parts of China,
386 particularly in NCP and TP. As one of the most densely populated regions in China, the prominent
387 increases in thermal indices in NCP indicate that the local has been experiencing increasing threats of
388 intensifying heat stress. Among the 12 indices, AT_{out} , HI, NET and WCT tend to have a slight cooling
389 trend in southeastern China. This cooling trend is consistent with the corresponding summer SAT.

390

391 The spatial distributions of the changing trends in winter across the mainland of China during 2003–2020
392 are depicted in Figure S7. The trend patterns in winter are similar to that in summer to some degrees. The

393 warming trends are concentrated in Southwest China, most parts of Northwest China, and parts of East
394 China (e.g., YRD). The cooling trends are located in TP, parts of Northeast and South China. The cooling
395 tendencies are especially significant in Northeast China, and most parts of Northwest and South China
396 (Figures S7 j&m). Parts of central China are seen with even stronger cooling thermal comfort.

397

398 In spring, increases in all thermal indices are observed in most parts of China (Figure S8), particularly in
399 northern regions, such as central Inner Mongolia, parts of NCP, and Northeast China, while parts of
400 southern China have slight decreases. These decreases are noticeable in NET and WCT (Figures S8 j&m).

401 In contrast to spring, the autumn season is observed with decreased thermal temperature in the north and
402 increases in the south (e.g., Southwest China, Figure S9).

403

404 **5 Discussion**

405 **5.1 Comparison with existing human thermal index datasets**

406 We compared our HITIC-Monthly with two existing datasets, i.e., HDI (Mistry, 2020) and HiTiSEA (Yan
407 et al., 2021), which have coarser spatial resolutions of $0.25^\circ \times 0.25^\circ$ and $0.1^\circ \times 0.1^\circ$ (Table 4), respectively.

408 We derived monthly mean AT_{in} in July 2018 from HDI and HiTiSEA and compared them with HITIC-
409 Monthly over the mainland of China, with a particular highlight in the four largest UAs, including
410 Beijing-Tianjin-Hebei (BTH), YRD, middle Yangtze River Valley (mYRV) and Pearl River Delta (PRD)
411 (Figure 14). The summer of 2018 was selected because it was included in all three datasets and frequent
412 heat events occurred in this summer (Zhou et al., 2020). Generally, the three datasets depict similar spatial
413 patterns. However, our HiTiSEA-Monthly dataset obviously provides more detailed and clearer spatial
414 information on human thermal stress than the other two. Additionally, the observed AT_{in} values at
415 individual weather stations are also compared (Figure 14). It can be seen that HDI and HiTiSEA
416 overestimate AT_{in} , and such overestimation is especially severe for HDI, while our dataset is in good
417 agreement with the observed AT_{in} at individual weather stations. Therefore, our predicted temperature
418 can describe the spatial variations in the city areas well, thereby providing fundamental support for fine-
419 scale climate studies, such as urban climate research.

420 **5.2 Limitations and future works**

421 There are 12 commonly used human thermal indices in the HiTIC-Monthly dataset produced in this study.
422 Nine of these indices were computed from temperature and humidity (or water vapor) and the other three
423 (i.e., AT_{out} , NET, and WCT) were derived from temperature, humidity, and wind speed. In addition, other
424 indices considering the combined effect of environmental variables such as sunlight (Blazejczyk, 1994;
425 Fanger, 1970; Höppe, 1999; Yaglou and Minaed, 1957) were proposed, including wet bulb globe
426 temperature (WBGT), predicted mean vote (PMV), UTCI, physiological equivalent temperature (PET),
427 etc. These thermal indices were not included in our study due to the lack of sunshine and radiative flux
428 data.

429

430 Since LST is the most important variable for predicting the 11 human thermal indices, the uncertainty in
431 the LST dataset may **influence** the accuracy of the human thermal indices. The LST variable in our
432 prediction is collected from a global seamless 1 km resolution daily LST dataset (Zhang et al., 2022b).
433 This dataset was generated based on spatiotemporal gap-filling algorithms and the MODIS LST data. It
434 may overestimate LST in some cases because the LST under cloudy weather was filled based on the data
435 in clear sky conditions (Zhang et al., 2022b). A high-quality LST dataset would further improve the
436 prediction accuracy of the human thermal indices.

437

438 The human thermal indices dataset is at a monthly scale, but the temporal resolution may not be sufficient
439 for the research of extreme weather events (e.g., heatwaves and cold spells) and related environmental
440 health (e.g., heat-related mortality). A daily high-resolution human thermal index collection (HiTIC-
441 Daily) will be produced and released in our future studies. In the current study, we provided the first
442 national-level dataset over the mainland of China with multiple high-resolution human thermal indices
443 in a monthly interval, which shows high prediction accuracies in all climate regimes across China. A
444 global dataset of multiple human thermal indices dataset is also expected in the near future.

445

446 **6 Data availability**

447 The high spatial resolution monthly human thermal index collection (HiTIC-Monthly) generated in this

448 study is freely available to the public in network common data form (NetCDF) at
449 <https://zenodo.org/record/6895533> (Zhang et al., 2022a). The human thermal indices include surface air
450 temperature (SAT), indoor Apparent Temperature (AT_{in}), outdoor shaded Apparent Temperature (AT_{out}),
451 Discomfort Index (DI), Effective Temperature (ET), Heat Index (HI), Humidex (HMI), Modified
452 Discomfort Index (MDI), Net Effective Temperature (NET), simplified Wet Bulb Globe Temperature
453 (sWBGT), Wet-Bulb Temperature (WBT), and Wind Chill Temperature (WCT). This dataset has a spatial
454 resolution of $1\text{ km} \times 1\text{ km}$ and covers the mainland of China from 2003 to 2020, stacking by year. Each
455 stack is composed of 12 monthly images. The unit of the dataset is 0.01 degree Celsius ($^{\circ}\text{C}$), and the
456 values are stored in an integer type (Int16) for saving storage space, and need to be divided by 100 to get
457 the values in degree Celsius when in use. The projection coordinate system is Albers Equal Area Conic
458 Projection. The naming rule and other detailed information can be found in “README.pdf”.

459

460 **7 Conclusions**

461 A long-term and high-resolution dataset of multiple human thermal indices is of great significance for
462 monitoring detailed spatiotemporal changes of human thermal stress in different climate regions across
463 China and assessing the health risks of people exposed to extreme heat at a fine scale. However, the
464 current datasets of human thermal indices (e.g., HDI and HiTiSEA) only have coarse spatial resolutions
465 ($> 0.1^{\circ}$). In this study, we generated a dataset of monthly human thermal index collection with a high
466 spatial resolution of 1 km over the mainland of China (HiTIC-Monthly). In this collection, 12 human
467 thermal indices from 2003 to 2020 were predicted, including SAT, AT_{in} , AT_{out} , DI, ET, HI, HMI, MDI,
468 NET, sWBGT, WBT, and WCT.

469

470 The HiTIC-Monthly dataset was produced by LGBM based on multi-source data, including MODIS LST,
471 DEM, land cover, population density, and impervious surface fraction. This dataset shows a desirable
472 performance, with mean R^2 , $RMSE$, MAE , and $Bias$ of 0.996, 0.693°C , 0.512°C , and 0.003°C ,
473 respectively. Our predictions also exhibit good agreements with the observations in both spatial and
474 temporal dimensions, demonstrating the broad applicability of our dataset. Moreover, the comparison
475 with two existing datasets (i.e., HDI and HiTiSEA) suggests that HiTIC-Monthly has more detailed

476 spatial information, indicating that our dataset can well support fine-scale studies. Further investigation
477 shows that almost all the indices show warming trends in most parts of China during 2003–2020,
478 particularly for North China, Southwest China, TP, and parts of Northwest China. Additionally, the
479 warming tendency is faster in spring and summer. WCT and NET show similar and strong cooling trends
480 in autumn and winter, while other indices exhibit slight long-term changes.

481

482 **Author contribution**

483 H.Z.: Data curation, Formal analysis, Investigation, Methodology, Writing – original draft preparation;
484 M.L.: Formal analysis, Conceptualization, Investigation, Funding acquisition, Methodology, Supervision
485 Writing – review & editing; Y.Z.: Formal analysis, Conceptualization, Investigation, Supervision,
486 Writing – review & editing; L.J.: Investigation, Writing – review & editing; E.G.: Investigation, Writing
487 – review & editing; Y.Y.: Investigation, Writing – review & editing; G.N.: Investigation, Writing – review
488 & editing; J.G.: Investigation, Writing – review & editing; Z.Z.: Investigation, Writing – review & editing;
489 K.G.: Investigation, Writing – review & editing; J.L.: Investigation, Writing – review & editing; X.L.:
490 Investigation, Writing – review & editing; S.W.: Investigation, Writing – review & editing; P.W.:
491 Investigation, Writing – review & editing; X.W.: Investigation, Writing – review & editing.

492

493 **Competing interests**

494 The authors declare that they have no conflict of interest.

495

496 **Acknowledgments**

497 This work was supported by the National Natural Science Foundation of China (41871029), the Natural
498 Science Foundation of Guangdong Province (2019A1515011025), the National Youth Talent Support
499 Program of China, the Pearl River Talent Recruitment Program of Guangdong Province
500 (2017GC010634), and the Innovation Group Project of Southern Marine Science and Engineering
501 Guangdong Laboratory (Zhuhai) (311021008). The authors are grateful to the editor and two reviewers
502 whose comments and suggestions have significantly improved the quality of our manuscript.

504 **References**

- 505 Abatzoglou, J. T., Dobrowski, S. Z., Parks, S. A., and Hegewisch, K. C.: TerraClimate, a high-resolution
 506 global dataset of monthly climate and climatic water balance from 1958-2015, *Sci Data*, 5, 170191,
 507 <https://doi.org/10.1038/sdata.2017.191>, 2018.
- 508 Arias, P., Bellouin, N., Coppola, E., Jones, R., Krinner, G., Marotzke, J., Naik, V., Palmer, M., Plattner,
 509 G.-K., and Rogelj, J.: Climate Change 2021: The Physical Science Basis. Contribution of Working
 510 Group14 I to the Sixth Assessment Report of the Intergovernmental Panel on Climate Change;
 511 Technical Summary, 2021.
- 512 Blazejczyk, K.: New climatological-and-physiological model of the human heat balance outdoor
 513 (MENEX) and its applications in bioclimatological studies in different scales, *Zeszyty IgiPZ PAN*,
 514 28, 27-58, 1994.
- 515 **Bolton, D.: The computation of equivalent potential temperature, *Monthly Weather Review*, 108, 1046-**
 516 **1053, 1980.**
- 517 Brake, R. and Bates, G.: A valid method for comparing rational and empirical heat stress indices, *The*
 518 *Annals of Occupational Hygiene*, 46, 165-174, <https://doi.org/10.1093/annhyg/mef030>, 2002.
- 519 Brimicombe, C., Di Napoli, C., Cornforth, R., Pappenberger, F., Petty, C., and Cloke, H. L.: Borderless
 520 Heat Hazards With Bordered Impacts, *Earth's Future*, 9, <https://doi.org/10.1029/2021ef002064>,
 521 2021.
- 522 Budhathoki, N. K. and Zander, K. K.: Socio-Economic Impact of and Adaptation to Extreme Heat and
 523 Cold of Farmers in the Food Bowl of Nepal, *International Journal of Environmental Research and*
 524 *Public Health*, 16, <https://doi.org/10.3390/ijerph16091578>, 2019.
- 525 Candido, C., Blanco, A. C., Medina, J., Gubatanga, E., Santos, A., Ana, R. S., and Reyes, R. B.:
 526 Improving the consistency of multi-temporal land cover mapping of Laguna lake watershed using
 527 light gradient boosting machine (LightGBM) approach, change detection analysis, and Markov
 528 chain, *Remote Sensing Applications: Society and Environment*, 23,
 529 <https://doi.org/10.1016/j.rsase.2021.100565>, 2021.
- 530 Di Napoli, C., Pappenberger, F., and Cloke, H. L.: Assessing heat-related health risk in Europe via the
 531 Universal Thermal Climate Index (UTCI), *International Journal of Biometeorology*, 62, 1155-1165,
 532 <https://doi.org/10.1007/s00484-018-1518-2>, 2018.
- 533 Di Napoli, C., Barnard, C., Prudhomme, C., Cloke, H. L., and Pappenberger, F.: ERA5-HEAT: A global
 534 gridded historical dataset of human thermal comfort indices from climate reanalysis, *Geoscience*
 535 *Data Journal*, 8, 2-10, <https://doi.org/10.1002/gdj3.102>, 2020.
- 536 Djongyang, N., Tchinda, R., and Njomo, D.: Thermal comfort: A review paper, *Renewable and*
 537 *Sustainable Energy Reviews*, 14, 2626-2640, <https://doi.org/10.1016/j.rser.2010.07.040>, 2010.
- 538 ECMWF: Copernicus Climate Change Service (C3S): ERA5: Fifth generation of ECMWF atmospheric
 539 reanalyses of the global climate. Copernicus Climate Change Service Climate Data Store (CDS),
 540 2017.
- 541 Enander, A. E. and Hygge, S.: Thermal stress and human performance, *Scand J Work Environ Health*, 16
 542 Suppl 1, 44-50, <https://doi.org/10.5271/sjweh.1823>, 1990.
- 543 Epstein, Y. and Moran, D. S.: Thermal comfort and the heat stress indices, *Ind Health*, 44, 388-398,

544 <https://doi.org/10.2486/indhealth.44.388>, 2006.

545 Fan, J., Ma, X., Wu, L., Zhang, F., Yu, X., and Zeng, W.: Light Gradient Boosting Machine: An efficient
546 soft computing model for estimating daily reference evapotranspiration with local and external
547 meteorological data, *Agricultural Water Management*, 225,
548 <https://doi.org/10.1016/j.agwat.2019.105758>, 2019.

549 Fang, C.: China's New Urbanization Developmental Paths, Blueprints and Patterns/Chuanglin Fang,
550 Danlin Yu, 2016.

551 Fanger, P. O.: Thermal comfort. Analysis and applications in environmental engineering, Thermal
552 comfort. Analysis and applications in environmental engineering., 1970.

553 Gagge, A. and Nishi, Y.: Physical indices of the thermal environment, *ASHRAE J.*;(United States), 18,
554 1976.

555 Gagge, A., Stolwijk, J. A., and Nishi, Y.: An effective temperature scale based on a simple model of
556 human physiological regulatory response, *Memoirs of the Faculty of Engineering, Hokkaido*
557 *University*, 13, 21-36, 1972.

558 Gaughan, A. E., Stevens, F. R., Linard, C., Jia, P., and Tatem, A. J.: High resolution population
559 distribution maps for Southeast Asia in 2010 and 2015, *PLoS One*, 8, e55882,
560 <https://doi.org/10.1371/journal.pone.0055882>, 2013.

561 Gong, P., Li, X., Wang, J., Bai, Y., Chen, B., Hu, T., Liu, X., Xu, B., Yang, J., Zhang, W., and Zhou, Y.:
562 Annual maps of global artificial impervious area (GAIA) between 1985 and 2018, *Remote Sensing*
563 *of Environment*, 236, <https://doi.org/10.1016/j.rse.2019.111510>, 2020.

564 Haines, A. and Ebi, K.: The Imperative for Climate Action to Protect Health, *The New England Journal*
565 *of Medicine*, 380, 263-273, <https://doi.org/10.1056/NEJMra1807873>, 2019.

566 He, Q., Wang, M., Liu, K., Li, K., and Jiang, Z.: GPRChinaTemp1km: a high-resolution monthly air
567 temperature dataset for China (1951–2020) based on machine learning, *Earth System Science Data*
568 *Discussions*, 1-29, 2021.

569 Hong, F., Zhan, W., Götsche, F.-M., Liu, Z., Dong, P., Fu, H., Huang, F., and Zhang, X.: A global dataset
570 of spatiotemporally seamless daily mean land surface temperatures: generation, validation, and
571 analysis, *Earth System Science Data*, 14, 3091-3113, <https://doi.org/10.5194/essd-14-3091-2022>,
572 2022.

573 Höppe, P.: The physiological equivalent temperature—a universal index for the biometeorological
574 assessment of the thermal environment, *International journal of Biometeorology*, 43, 71-75, 1999.

575 Houghton, F. C. and Yaglou, C. P.: Determining equal comfortlines, *ASHVE Trans.*, 29, 165-176, 1923.

576 IPCC: Climate Change 2021: The Physical Science Basis. Contribution of Working Group I to the Sixth
577 Assessment Report of the Intergovernmental Panel on Climate Change, 2021.

578 Kang, S. and Eltahir, E. A. B.: North China Plain threatened by deadly heatwaves due to climate change
579 and irrigation, *Nature Communications*, 9, 2894, <https://doi.org/10.1038/s41467-018-05252-y>,
580 2018.

581 Ke, G., Meng, Q., Finley, T., Wang, T., Chen, W., Ma, W., Ye, Q., and Liu, T.-Y.: Lightgbm: A highly
582 efficient gradient boosting decision tree, *Advances in neural information processing systems*, 30,
583 2017.

584 Krzysztof, B., Pavol, N., Oleh, S., Agnieszka, H., Olesya, S., Anna, B., and Katarina, M.: Influence of
585 geographical factors on thermal stress in northern Carpathians, *International Journal of*
586 *Biometeorology*, 65, 1553-1566, <https://doi.org/10.1007/s00484-020-02011-x>, 2021.

587 Kuchcik, M.: Mortality and thermal environment (UTCI) in Poland-long-term, multi-city study,

588 International Journal of Biometeorology 65, 1529-1541, [https://doi.org/10.1007/s00484-020-](https://doi.org/10.1007/s00484-020-01995-w)
589 [01995-w](https://doi.org/10.1007/s00484-020-01995-w), 2021.

590 Lazaro, P. and Momayez, M.: Heat Stress in Hot Underground Mines: a Brief Literature Review, Mining,
591 Metallurgy & Exploration, 38, 497-508, <https://doi.org/10.1007/s42461-020-00324-4>, 2020.

592 Li, J., Chen, Y. D., Gan, T. Y., and Lau, N.-C.: Elevated increases in human-perceived temperature under
593 climate warming, Nature Climate Change, 8, 43-47, <https://doi.org/10.1038/s41558-017-0036-2>,
594 2018.

595 Li, Q., Liu, X., Zhang, H., Thomas C. P., and David R, E.: Detecting and adjusting temporal
596 inhomogeneity in Chinese mean surface air temperature data, Advances in Atmospheric Sciences,
597 21, 260-268, <https://doi.org/10.1007/bf02915712>, 2004.

598 Li, W., Hao, X., Wang, L., Li, Y., Li, J., Li, H., and Han, T.: Detection and Attribution of Changes in
599 Thermal Discomfort over China during 1961–2014 and Future Projections, Advances in
600 Atmospheric Sciences, 39, 456-470, <https://doi.org/10.1007/s00376-021-1168-x>, 2022.

601 Liu, X., Guo, J., Zhang, A., Zhou, J., Chu, Z., Zhou, Y., and Ren, G.: Urbanization Effects on Observed
602 Surface Air Temperature Trends in North China, Journal of Climate, 21, 1333-1348,
603 <https://doi.org/10.1175/2007jcli1348.1>, 2008.

604 Los, H., Mendes, G. S., Cordeiro, D., Grosso, N., Costa, H., Benevides, P., and Caetano, M.: Evaluation
605 of Xgboost and Lgbm Performance in Tree Species Classification with Sentinel-2 Data, 2021 IEEE
606 International Geoscience and Remote Sensing Symposium IGARSS,
607 <https://doi.org/10.1109/igarss47720.2021.9553031>, 2021.

608 Luo, M. and Lau, N.-C.: Characteristics of summer heat stress in China during 1979–2014: climatology
609 and long-term trends, Climate Dynamics, 53, 5375-5388, [https://doi.org/10.1007/s00382-019-](https://doi.org/10.1007/s00382-019-04871-5)
610 [04871-5](https://doi.org/10.1007/s00382-019-04871-5), 2019.

611 Luo, M. and Lau, N. C.: Increasing Human-Perceived Heat Stress Risks Exacerbated by Urbanization in
612 China: A Comparative Study Based on Multiple Metrics, Earth's Future, 9,
613 <https://doi.org/10.1029/2020ef001848>, 2021.

614 Luo, M., Lau, N. C., Liu, Z., Wu, S., and Wang, X.: An Observational Investigation of Spatiotemporally
615 Contiguous Heatwaves in China From a 3D Perspective, Geophysical Research Letters, 49,
616 <https://doi.org/10.1029/2022gl097714>, 2022.

617 Masterton, J. M., Richardson, F. A., and atmosphérique, C. S. d. l. e.: Humidex: A Method of Quantifying
618 Human Discomfort Due to Excessive Heat and Humidity, Service de l'environnement
619 atmosphérique.1979.

620 McCarty, D. A., Kim, H. W., and Lee, H. K.: Evaluation of Light Gradient Boosted Machine Learning
621 Technique in Large Scale Land Use and Land Cover Classification, Environments, 7,
622 <https://doi.org/10.3390/environments7100084>, 2020.

623 Mistry, M. N.: A High Spatiotemporal Resolution Global Gridded Dataset of Historical Human
624 Discomfort Indices, Atmosphere, 11, <https://doi.org/10.3390/atmos11080835>, 2020.

625 Moda, H. M., Filho, W. L., and Minhas, A.: Impacts of Climate Change on Outdoor Workers and their
626 Safety: Some Research Priorities, International Journal of Environmental Research and Public
627 Health, 16, <https://doi.org/10.3390/ijerph16183458>, 2019.

628 Moran, D., Shapiro, Y., Epstein, Y., Matthew, W., and Pandolf, K.: A modified discomfort index (MDI)
629 as an alternative to the wet bulb globe temperature (WBGT), Environmental Ergonomics VIII,
630 Hodgdon JA, Heaney JH, Buono MJ (Eds.), 77-80, 1998.

631 Nastos, P. T. and Matzarakis, A.: The effect of air temperature and human thermal indices on mortality

632 in Athens, Greece, *Theoretical and Applied Climatology*, 108, 591-599,
633 <https://doi.org/10.1007/s00704-011-0555-0>, 2011.

634 NWS: Meteorological Conversions and Calculations: Heat Index Calculator, 2011.

635 Osczevski, R. and Bluestein, M.: The New Wind Chill Equivalent Temperature Chart, *Bulletin of the*
636 *American Meteorological Society*, 86, 1453-1458, <https://doi.org/10.1175/bams-86-10-1453>, 2005.

637 Patz, J. A., Campbell-Lendrum, D., Holloway, T., and Foley, J. A.: Impact of regional climate change on
638 human health, *Nature*, 438, 310-317, <https://doi.org/10.1038/nature04188>, 2005.

639 Peng, S., Ding, Y., Liu, W., and Li, Z.: 1 km monthly temperature and precipitation dataset for China
640 from 1901 to 2017, *Earth System Science Data*, 11, 1931-1946, [https://doi.org/10.5194/essd-11-](https://doi.org/10.5194/essd-11-1931-2019)
641 [1931-2019](https://doi.org/10.5194/essd-11-1931-2019), 2019.

642 Periard, J. D., Eijssvogels, T. M. H., and Daanen, H. A. M.: Exercise under heat stress: thermoregulation,
643 hydration, performance implications, and mitigation strategies, *Physiol Rev*, 101, 1873-1979,
644 <https://doi.org/10.1152/physrev.00038.2020>, 2021.

645 Rahman, M. A., Franceschi, E., Pattnaik, N., Moser-Reischl, A., Hartmann, C., Paeth, H., Pretzsch, H.,
646 Rotzer, T., and Pauleit, S.: Spatial and temporal changes of outdoor thermal stress: influence of
647 urban land cover types, *Sci Rep*, 12, 671, <https://doi.org/10.1038/s41598-021-04669-8>, 2022.

648 Raymond, C., Matthews, T., and Horton, R. M.: The emergence of heat and humidity too severe for
649 human tolerance, *Science Advances*, 6, eaaw1838, <https://doi.org/10.1126/sciadv.aaw1838>, 2020.

650 Ren, Z., Fu, Y., Dong, Y., Zhang, P., and He, X.: Rapid urbanization and climate change significantly
651 contribute to worsening urban human thermal comfort: A national 183-city, 26-year study in China,
652 *Urban Climate*, 43, <https://doi.org/10.1016/j.uclim.2022.101154>, 2022.

653 **Rice, J. A.: *Mathematical statistics and data analysis*, Cengage Learning, 2006.**

654 Rogers, C. D. W., Ting, M., Li, C., Kornhuber, K., Coffel, E. D., Horton, R. M., Raymond, C., and Singh,
655 D.: Recent Increases in Exposure to Extreme Humid-Heat Events Disproportionately Affect
656 Populated Regions, *Geophysical Research Letters*, 48, <https://doi.org/10.1029/2021gl094183>, 2021.

657 Roghanchi, P. and Kocsis, K. C.: Challenges in Selecting an Appropriate Heat Stress Index to Protect
658 Workers in Hot and Humid Underground Mines, *Saf Health Work*, 9, 10-16,
659 <https://doi.org/10.1016/j.shaw.2017.04.002>, 2018.

660 Rothfus, L. P. and Headquarters, N. S. R.: The heat index equation (or, more than you ever wanted to
661 know about heat index), Fort Worth, Texas: National Oceanic and Atmospheric Administration,
662 National Weather Service, Office of Meteorology, 9023, 1990.

663 Rustemeyer, N. and Howells, M.: Excess Mortality in England during the 2019 Summer Heatwaves,
664 *Climate*, 9, <https://doi.org/10.3390/cli9010014>, 2021.

665 Schwingshackl, C., Sillmann, J., Vicedo-Cabrera, A. M., Sandstad, M., and Aunan, K.: Heat Stress
666 Indicators in CMIP6: Estimating Future Trends and Exceedances of Impact-Relevant Thresholds,
667 *Earth's Future*, 9, <https://doi.org/10.1029/2020ef001885>, 2021.

668 Sohar, E., Adar, R., and Kaly, J.: Comparison of the environmental heat load in various parts of Israel,
669 *ISRAEL JOURNAL OF EXPERIMENTAL MEDICINE*, 10, 111-&, 1963.

670 Staiger, H., Laschewski, G., and Matzarakis, A.: Selection of Appropriate Thermal Indices for
671 Applications in Human Biometeorological Studies, *Atmosphere*, 10,
672 <https://doi.org/10.3390/atmos10010018>, 2019.

673 Steadman, R. G.: The assessment of sultriness. Part I: A temperature-humidity index based on human
674 physiology and clothing science, *Journal of Applied Meteorology and Climatology*, 18, 861-873,
675 1979.

676 Steadman, R. G.: A universal scale of apparent temperature, *Journal of Applied Meteorology and*
677 *Climatology*, 23, 1674-1687, 1984.

678 Stolwijk, J.: Heat exchangers between body and environment, *Bibliotheca Radiologica*, 144-150, 1975.

679 Stull, R.: Wet-Bulb Temperature from Relative Humidity and Air Temperature, *Journal of Applied*
680 *Meteorology and Climatology*, 50, 2267-2269, <https://doi.org/10.1175/jamc-d-11-0143.1>, 2011.

681 Su, H., Wang, A., Zhang, T., Qin, T., Du, X., and Yan, X.-H.: Super-resolution of subsurface temperature
682 field from remote sensing observations based on machine learning, *International Journal of Applied*
683 *Earth Observation and Geoinformation*, 102, <https://doi.org/10.1016/j.jag.2021.102440>, 2021.

684 Su, Y.: Prediction of air quality based on Gradient Boosting Machine Method, 2020 International
685 Conference on Big Data and Informatization Education (ICBDIE),
686 <https://doi.org/10.1109/icbdie50010.2020.00099>, 2020.

687 Sulla-Menashe, D. and Friedl, M.: MCD12Q1 MODIS/Terra+ Aqua Land Cover Type Yearly L3 Global
688 500m SIN Grid V006, NASA EOSDIS Land Processes DAAC: Sioux Falls, SD, USA,
689 <https://doi.org/10.5067/MODIS/MCD12Q1.006>, 2019.

690 Sun, Q., Miao, C., Hanel, M., Borthwick, A. G. L., Duan, Q., Ji, D., and Li, H.: Global heat stress on
691 health, wildfires, and agricultural crops under different levels of climate warming, *Environment*
692 *International*, 128, 125-136, <https://doi.org/10.1016/j.envint.2019.04.025>, 2019.

693 Szer, I., Lipecki, T., Szer, J., and Czarnocki, K.: Using meteorological data to estimate heat stress of
694 construction workers on scaffolds for improved safety standards, *Automation in Construction*, 134,
695 <https://doi.org/10.1016/j.autcon.2021.104079>, 2022.

696 Tamiminia, H., Salehi, B., Mahdianpari, M., Beier, C. M., Johnson, L., and Phoenix, D. B.: A Comparison
697 of Random Forest and Light Gradient Boosting Machine for Forest above-Ground Biomass
698 Estimation Using a Combination of Landsat, Alos Palsar, and Airborne Lidar Data, *The*
699 *International Archives of the Photogrammetry, Remote Sensing and Spatial Information Sciences*,
700 XLIV-M-3-2021, 163-168, <https://doi.org/10.5194/isprs-archives-XLIV-M-3-2021-163-2021>,
701 2021.

702 Tian, H., Zhao, Y., Luo, M., He, Q., Han, Y., and Zeng, Z.: Estimating PM_{2.5} from multisource data: A
703 comparison of different machine learning models in the Pearl River Delta of China, *Urban Climate*,
704 35, <https://doi.org/10.1016/j.uclim.2020.100740>, 2021.

705 Tian, P., Lu, H., Li, D., and Guan, Y.: Quantifying the effects of meteorological change between
706 neighboring days on human thermal comfort in China, *Theoretical and Applied Climatology*, 147,
707 1345-1357, <https://doi.org/10.1007/s00704-021-03908-2>, 2022.

708 Tong, S., Prior, J., McGregor, G., Shi, X., and Kinney, P.: Urban heat: an increasing threat to global health,
709 *BMJ*, 375, n2467, <https://doi.org/10.1136/bmj.n2467>, 2021.

710 Tuholske, C., Caylor, K., Funk, C., Verdin, A., Sweeney, S., Grace, K., Peterson, P., and Evans, T.: Global
711 urban population exposure to extreme heat, *Proc Natl Acad Sci U S A*, 118,
712 <https://doi.org/10.1073/pnas.2024792118>, 2021.

713 United Nations: World population prospects, Multimedia Library, 2017.

714 Varentsov, M., Shartova, N., Grischenko, M., and Konstantinov, P.: Spatial Patterns of Human Thermal
715 Comfort Conditions in Russia: Present Climate and Trends, *Weather, Climate, and Society*, 12, 629-
716 642, <https://doi.org/10.1175/wcas-d-19-0138.1>, 2020.

717 Wang, C., Zhan, W., Liu, Z., Li, J., Li, L., Fu, P., Huang, F., Lai, J., Chen, J., Hong, F., and Jiang, S.:
718 Satellite-based mapping of the Universal Thermal Climate Index over the Yangtze River Delta
719 urban agglomeration, *Journal of Cleaner Production*, 277,

720 <https://doi.org/10.1016/j.jclepro.2020.123830>, 2020.

721 Wang, F., Duan, K., and Zou, L.: Urbanization Effects on Human-Perceived Temperature Changes in the
722 North China Plain, *Sustainability*, 11, <https://doi.org/10.3390/su11123413>, 2019.

723 Wang, P., Luo, M., Liao, W., Xu, Y., Wu, S., Tong, X., Tian, H., Xu, F., and Han, Y.: Urbanization
724 contribution to human perceived temperature changes in major urban agglomerations of China,
725 *Urban Climate*, 38, <https://doi.org/10.1016/j.uclim.2021.100910>, 2021.

726 Xu, W., Li, Q., Wang, X. L., Yang, S., Cao, L., and Feng, Y.: Homogenization of Chinese daily surface
727 air temperatures and analysis of trends in the extreme temperature indices, *Journal of Geophysical
728 Research: Atmospheres*, 118, 9708-9720, <https://doi.org/10.1002/jgrd.50791>, 2013.

729 Yaglou, C. and Minaed, D.: Control of heat casualties at military training centers, *Arch. Indust. Health*,
730 16, 302-316, 1957.

731 Yamazaki, D., Ikeshima, D., Tawatari, R., Yamaguchi, T., O'Loughlin, F., Neal, J. C., Sampson, C. C.,
732 Kanae, S., and Bates, P. D.: A high-accuracy map of global terrain elevations, *Geophysical Research
733 Letters*, 44, 5844-5853, <https://doi.org/10.1002/2017gl072874>, 2017.

734 Yan, Y., Xu, Y., and Yue, S.: A high-spatial-resolution dataset of human thermal stress indices over South
735 and East Asia, *Sci Data*, 8, 229, <https://doi.org/10.1038/s41597-021-01010-w>, 2021.

736 Yan, Y. Y.: Human Thermal Climates in China, *Physical Geography*, 26, 163-176,
737 <https://doi.org/10.2747/0272-3646.26.3.163>, 2013.

738 Zeng, Z., Gui, K., Wang, Z., Luo, M., Geng, H., Ge, E., An, J., Song, X., Ning, G., Zhai, S., and Liu, H.:
739 Estimating hourly surface PM_{2.5} concentrations across China from high-density meteorological
740 observations by machine learning, *Atmospheric Research*, 254,
741 <https://doi.org/10.1016/j.atmosres.2021.105516>, 2021.

742 Zeng, Z., Ziegler, A. D., Searchinger, T., Yang, L., Chen, A., Ju, K., Piao, S., Li, L. Z. X., Ciais, P., Chen,
743 D., Liu, J., Azorin-Molina, C., Chappell, A., Medvigy, D., and Wood, E. F.: A reversal in global
744 terrestrial stilling and its implications for wind energy production, *Nature Climate Change*, 9, 979-
745 985, <https://doi.org/10.1038/s41558-019-0622-6>, 2019.

746 Zhang, G., Azorin-Molina, C., Chen, D., McVicar, T. R., Guijarro, J. A., Kong, F., Minola, L., Deng, K.,
747 and Shi, P.: Uneven Warming Likely Contributed to Declining Near-Surface Wind Speeds in
748 Northern China Between 1961 and 2016, *Journal of Geophysical Research: Atmospheres*, 126,
749 <https://doi.org/10.1029/2020jd033637>, 2021.

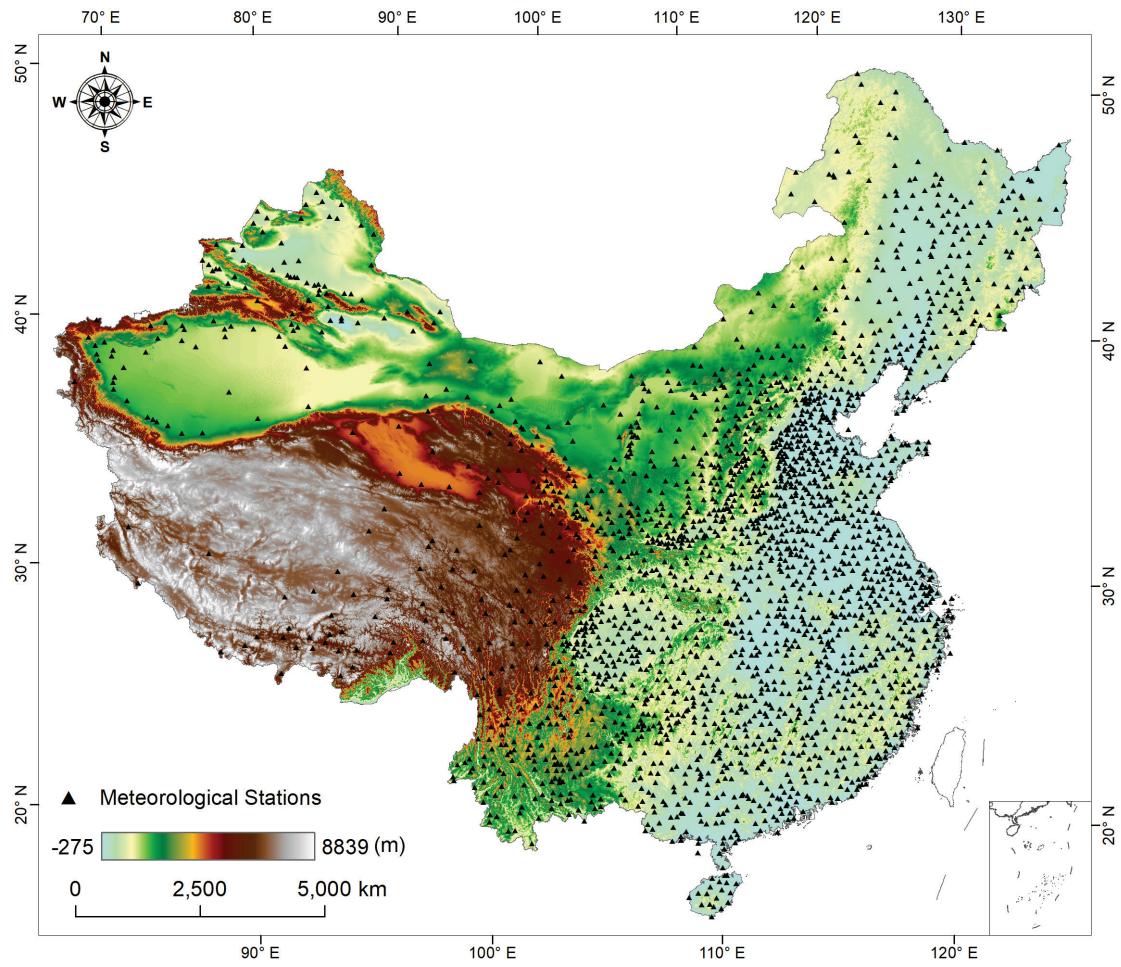
750 Zhang, H., Luo, M., Zhao, Y., Lin, L., Ge, E., Yang, Y., Ning, G., Zeng, Z., Gui, K., Li, J., Chan, T. O.,
751 Li, X., Wu, S., Wang, P., and Wang, X.: HiTIC-Monthly: A Monthly High Spatial Resolution (1 km)
752 Human Thermal Index Collection over China during 2003–2020 (1.0), Zenodo [dataset],
753 <https://doi.org/10.5281/zenodo.6895533>, 2022a.

754 Zhang, T., Zhou, Y., Zhu, Z., Li, X., and Asrar, G. R.: A global seamless 1 km resolution daily land surface
755 temperature dataset (2003–2020), *Earth System Science Data*, 14, 651-664,
756 <https://doi.org/10.5194/essd-14-651-2022>, 2022b.

757 Zhao, B., Mao, K., Cai, Y., Shi, J., Li, Z., Qin, Z., Meng, X., Shen, X., and Guo, Z.: A combined Terra
758 and Aqua MODIS land surface temperature and meteorological station data product for China from
759 2003 to 2017, *Earth System Science Data*, 12, 2555-2577, [https://doi.org/10.5194/essd-12-2555-
760 2020](https://doi.org/10.5194/essd-12-2555-2020), 2020.

761 Zhao, C., Liu, B., Piao, S., Wang, X., Lobell, D. B., Huang, Y., Huang, M., Yao, Y., Bassu, S., Ciais, P.,
762 Durand, J. L., Elliott, J., Ewert, F., Janssens, I. A., Li, T., Lin, E., Liu, Q., Martre, P., Muller, C.,
763 Peng, S., Penuelas, J., Ruane, A. C., Wallach, D., Wang, T., Wu, D., Liu, Z., Zhu, Y., Zhu, Z., and

764 Asseng, S.: Temperature increase reduces global yields of major crops in four independent estimates,
765 Proc Natl Acad Sci U S A, 114, 9326-9331, <https://doi.org/10.1073/pnas.1701762114>, 2017.
766 Zhao, Y. and Zhu, Z.: ASI: An artificial surface Index for Landsat 8 imagery, International Journal of
767 Applied Earth Observation and Geoinformation, 107, 10.1016/j.jag.2022.102703, 2022.
768 Zhou, C., Chen, D., Wang, K., Dai, A., and Qi, D.: Conditional Attribution of the 2018 Summer Extreme
769 Heat over Northeast China: Roles of Urbanization, Global Warming, and Warming-Induced
770 Circulation Changes, Bulletin of the American Meteorological Society, 101, S71-S76,
771 <https://doi.org/10.1175/bams-d-19-0197.1>, 2020.
772

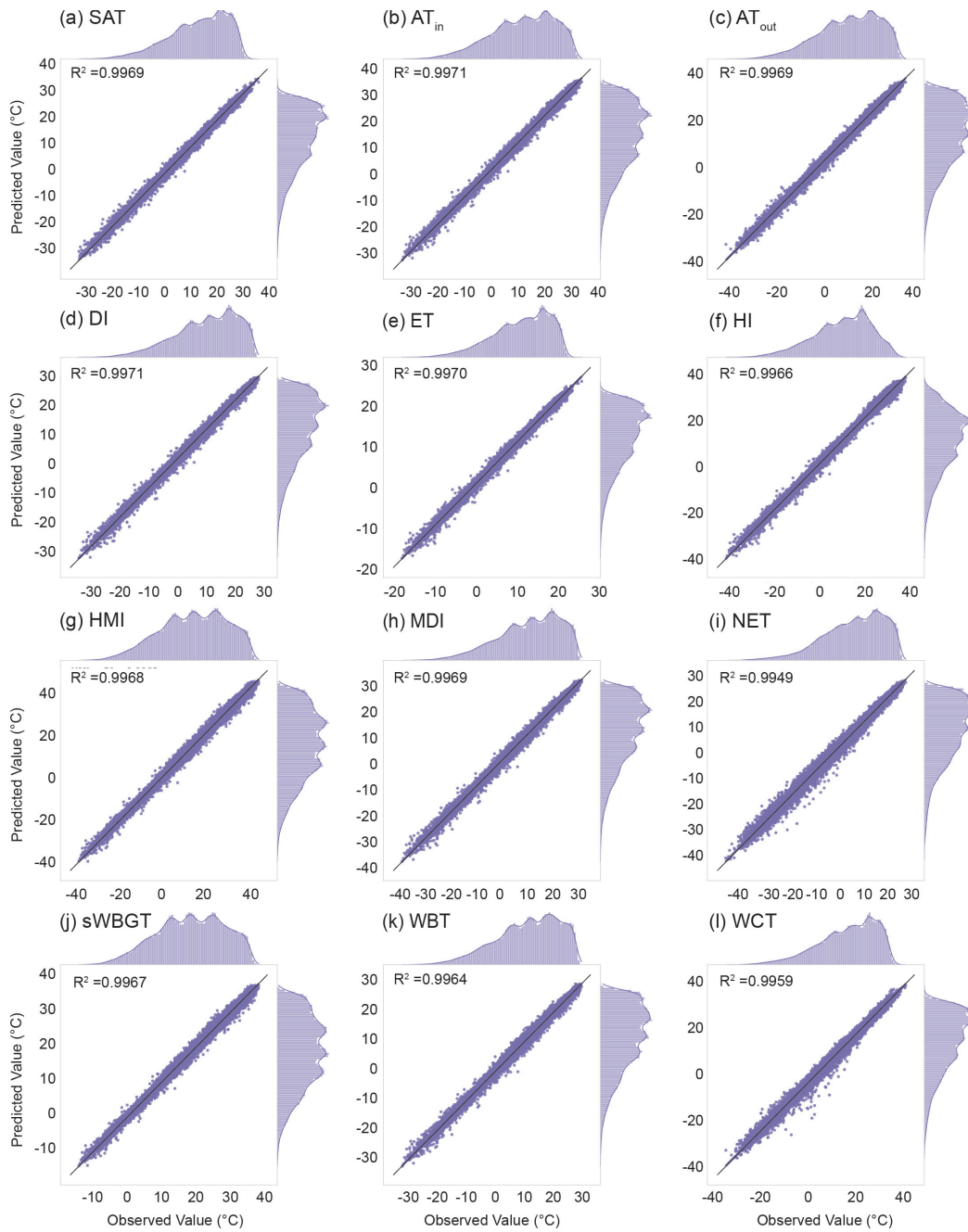


774

775 **Figure 1. Spatial distribution of meteorological stations in the mainland of China, with color shadings**

776 **indicating the elevation in meters.**

777



778

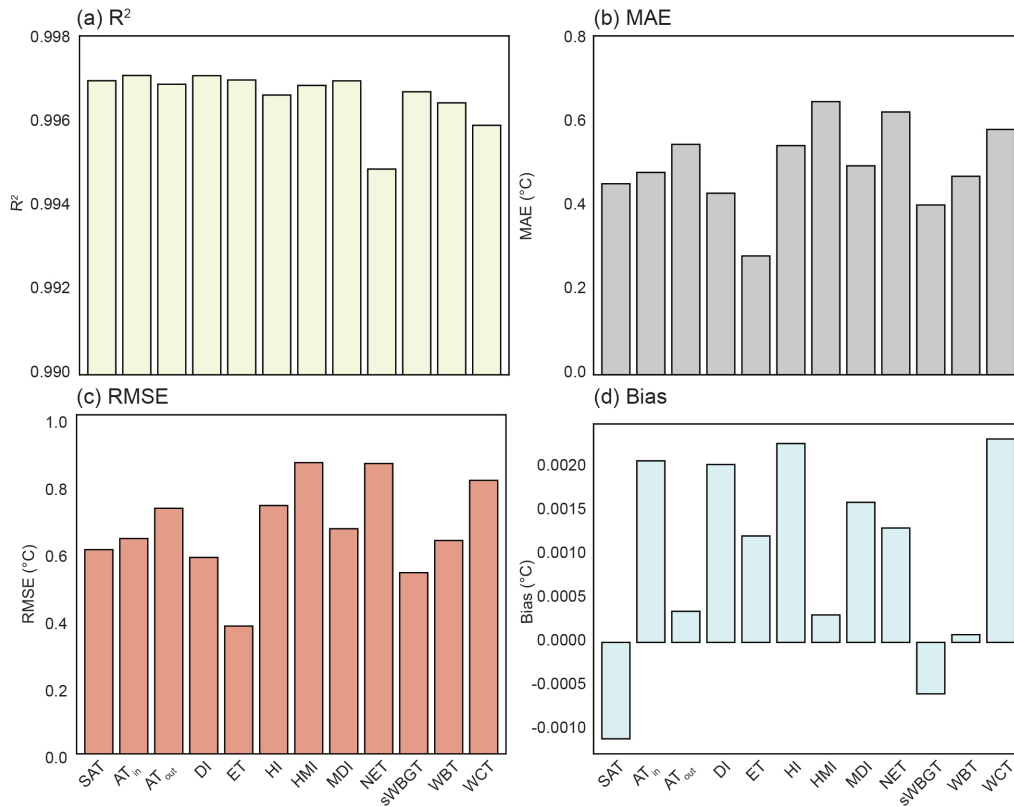
779

780

781

782

Figure 2. Scatter plots of predictions versus observations of the 12 human thermal indices over the mainland of China during 2003–2020. (a) SAT, (b) AT_{in} , (c) AT_{out} , (d) DI, (e) ET, (f) HI, (g) HMI, (h) MDI, (i) NET, (j) sWBGT, (k) WBT, and (l) WCT.



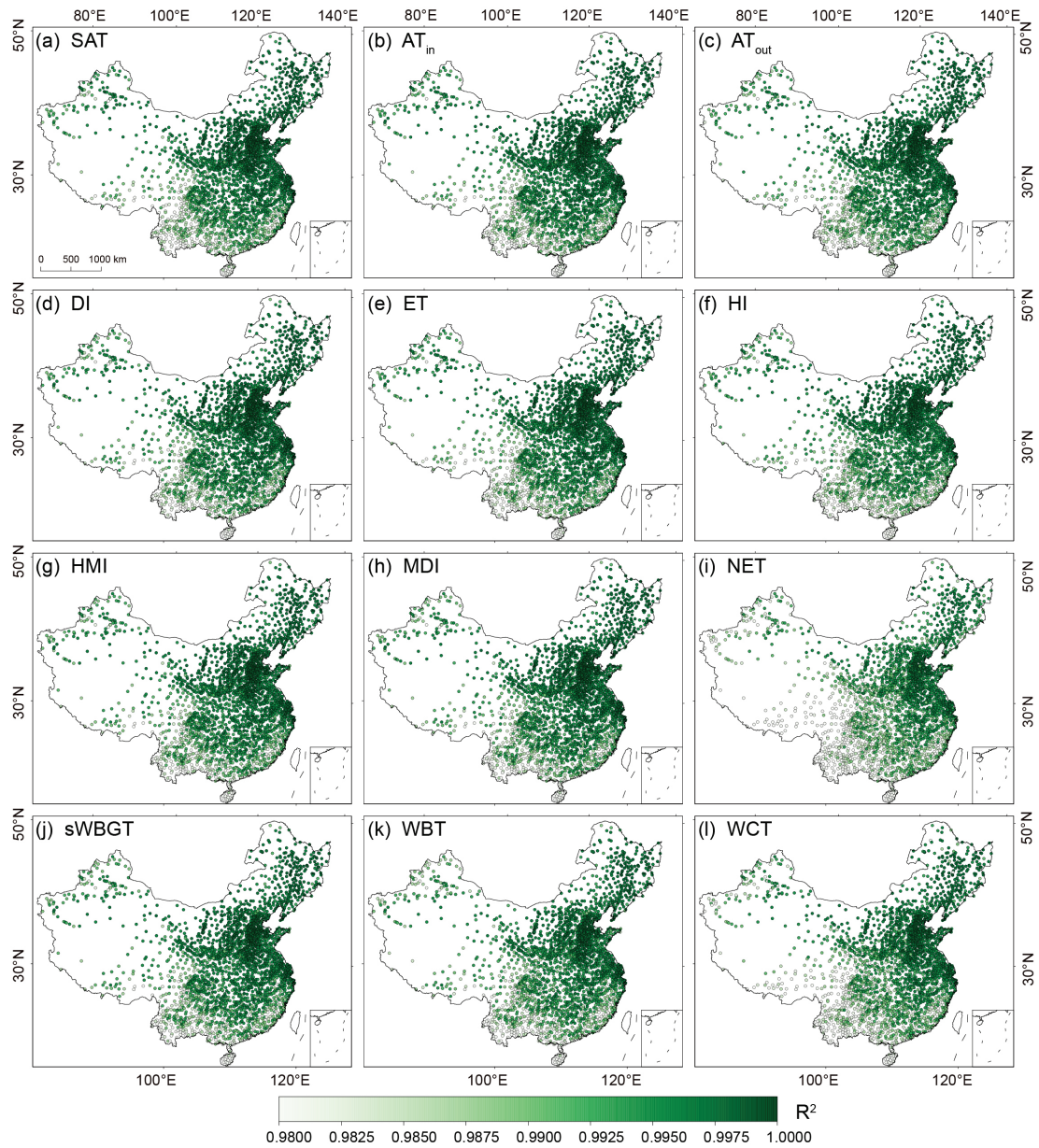
783

784

785

786

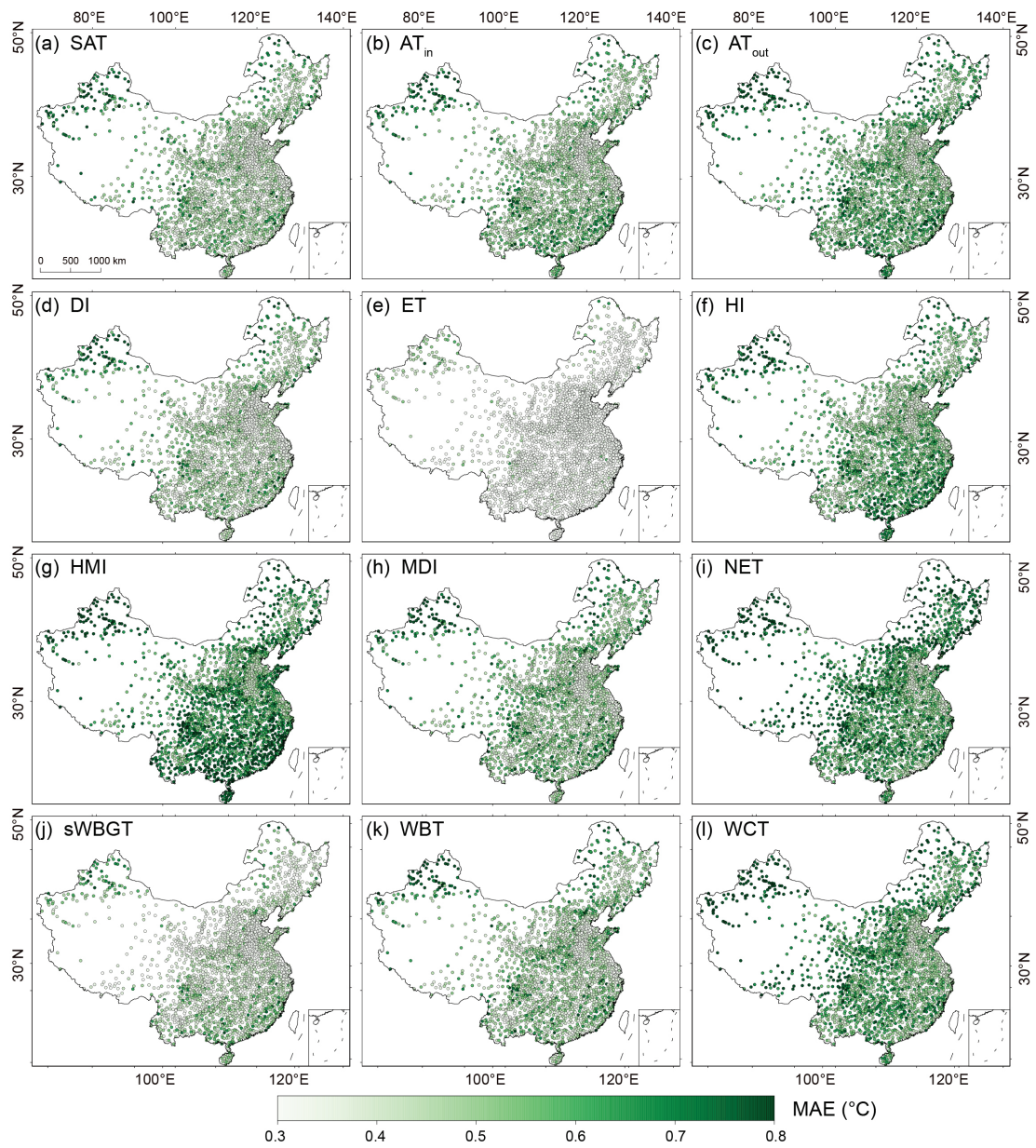
Figure 3. Overall prediction accuracies of the 12 human thermal indices over the mainland of China during 2003–2020. (a) R^2 , (b) MAE, (c) RMSE, (d) Bias.



787

788 **Figure 4. Spatial distribution of R^2 of the 12 human thermal index predictions at individual meteorological**
 789 **stations over the mainland of China during 2003–2020.**

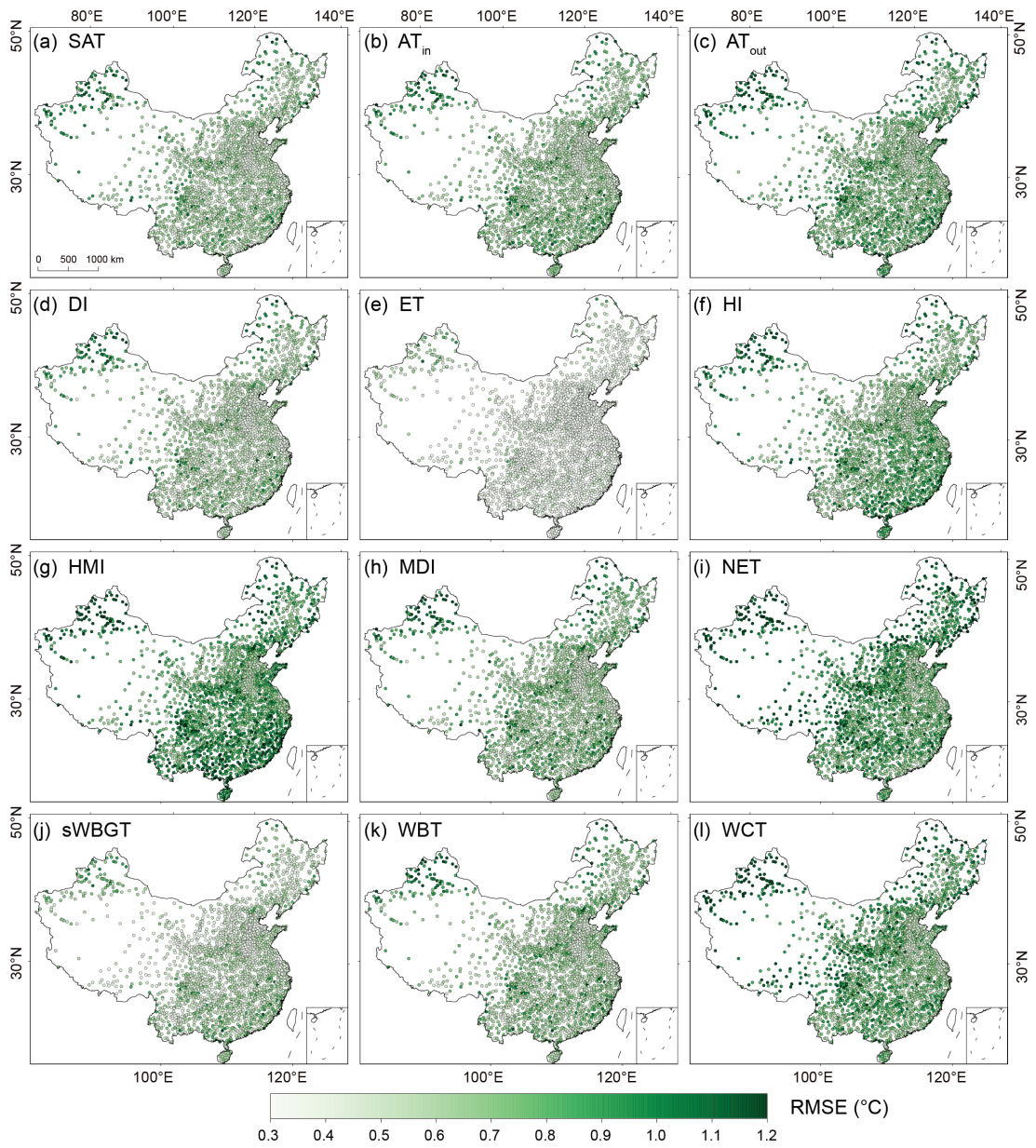
790



791

792 **Figure 5. As Figure 4 but for MAE.**

793

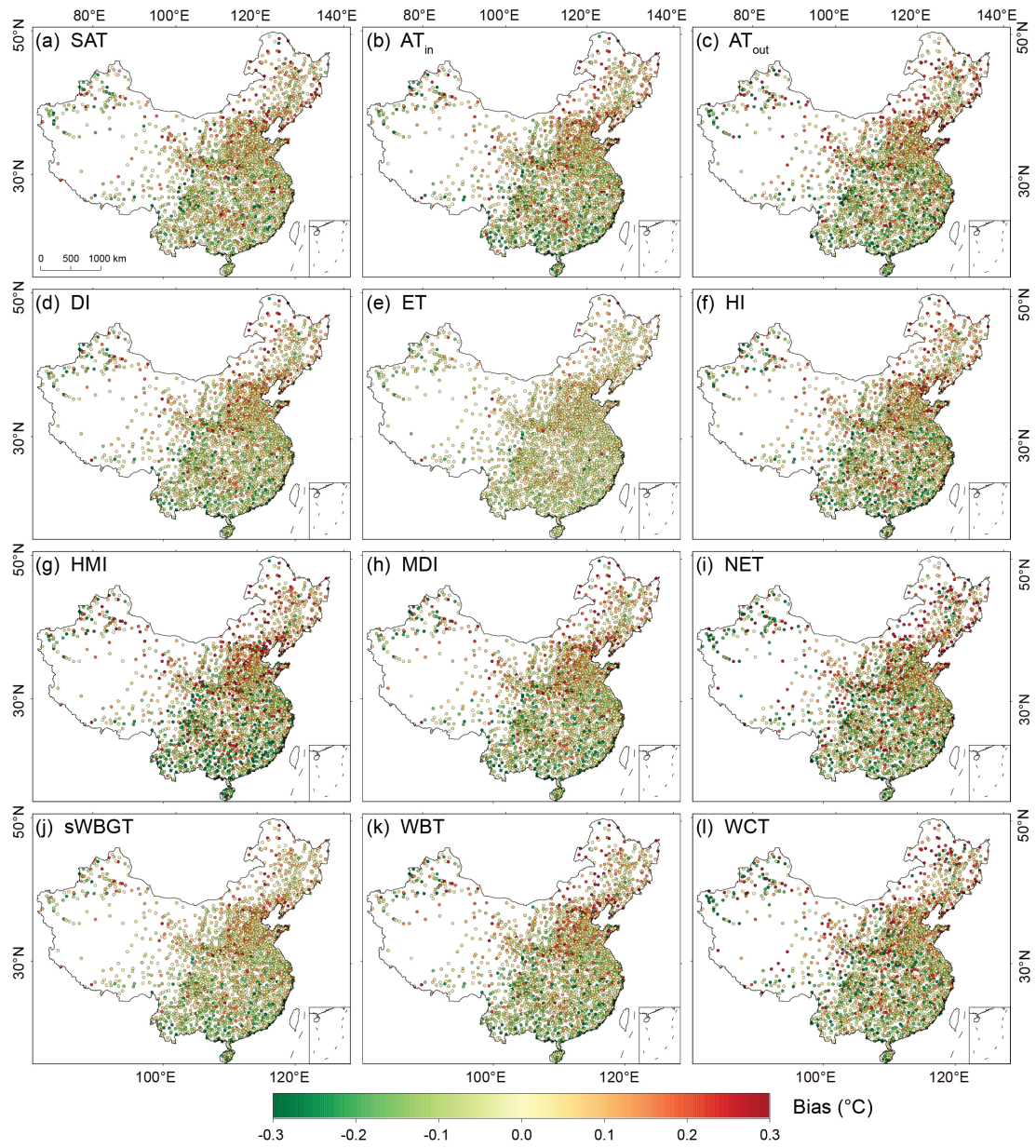


794

795

Figure 6. As Figure 4 but for *RMSE*.

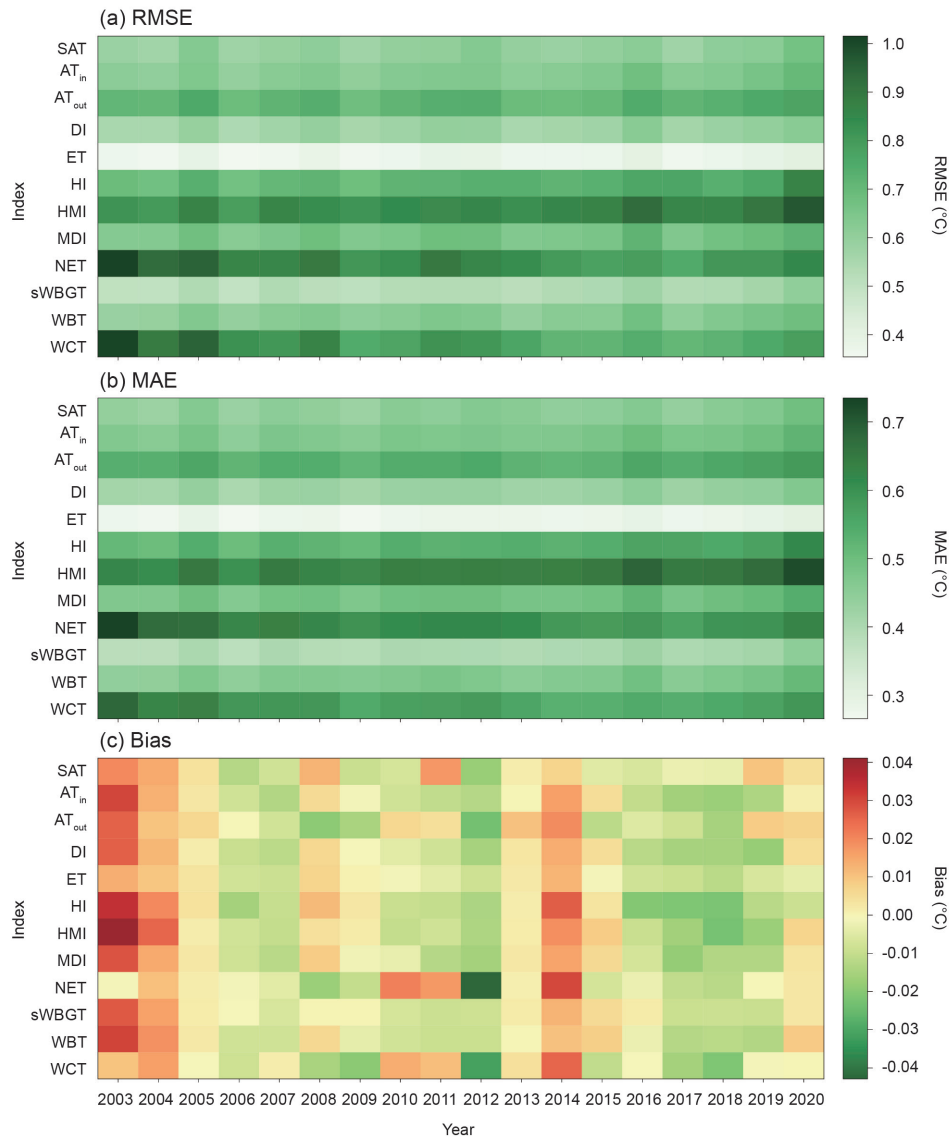
796



797

798 **Figure 7. As Figure 4 but for *Bias*.**

799

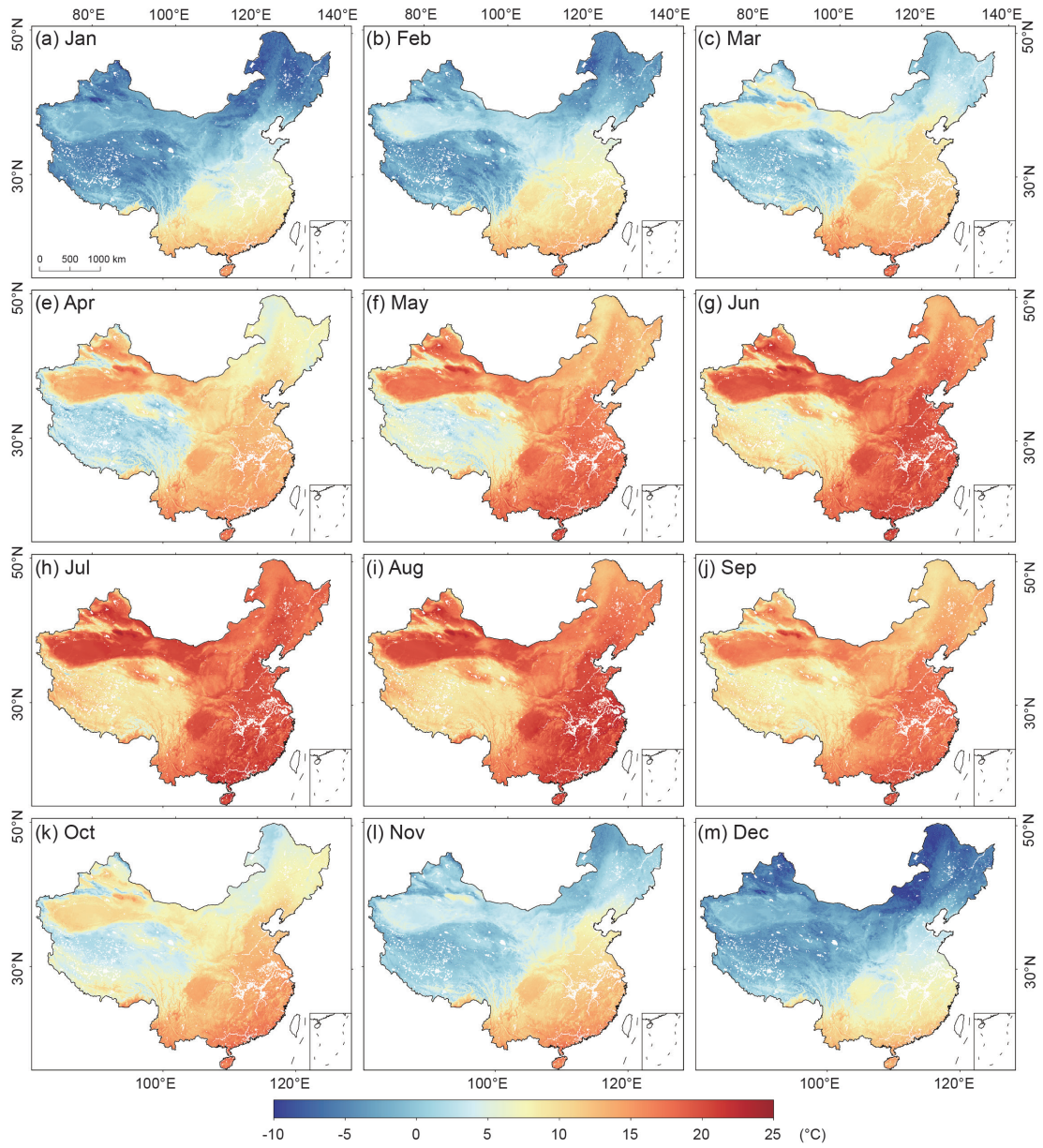


800

801 **Figure 8. Annual prediction accuracies of the 12 human thermal indices over the mainland of China during**

802 **2003–2020: (a) RMSE, (b) MAE, (c) Bias.**

803

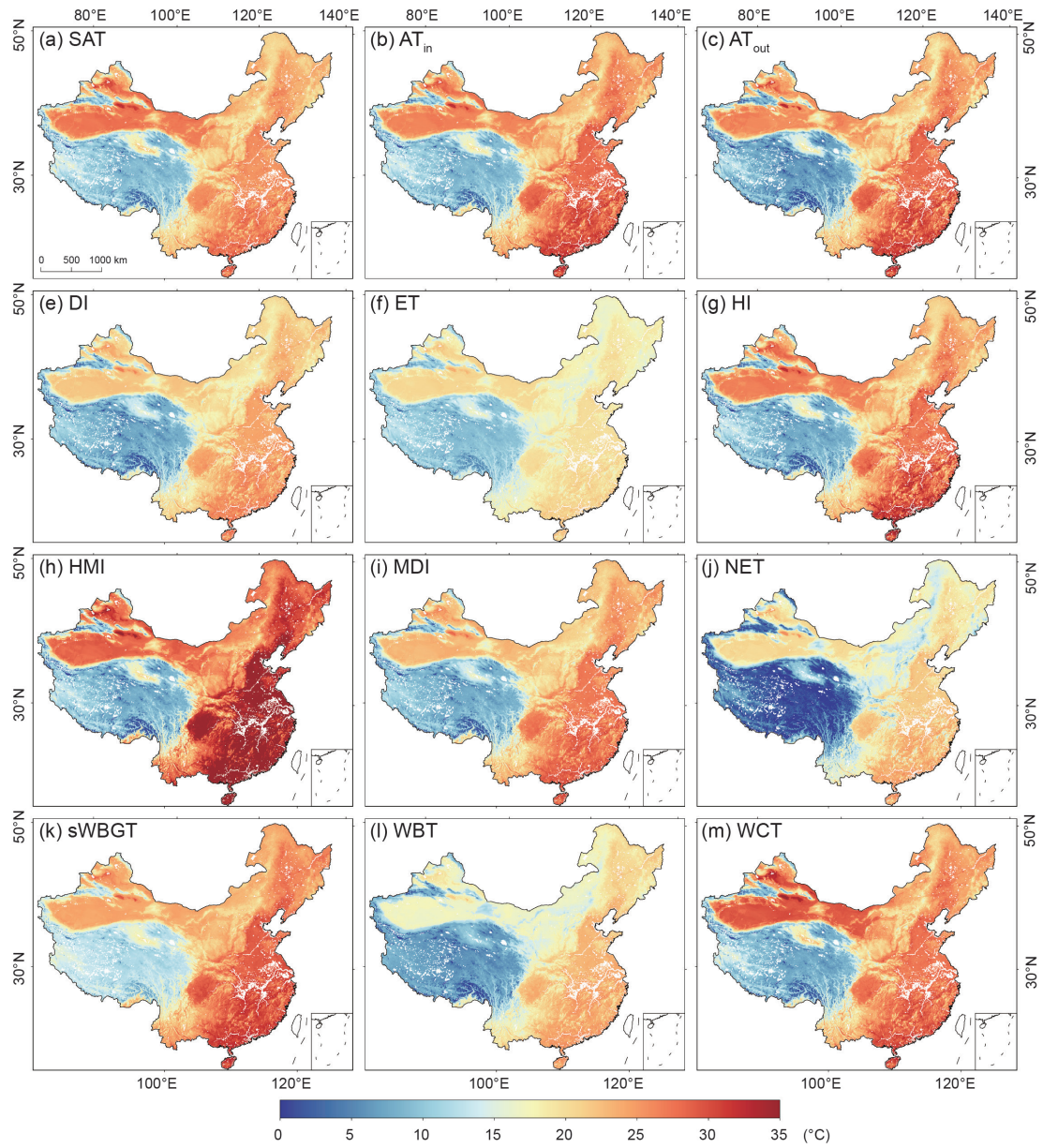


804

805

Figure 9. Spatial distributions of the monthly mean ET over the mainland of China in 2020.

806



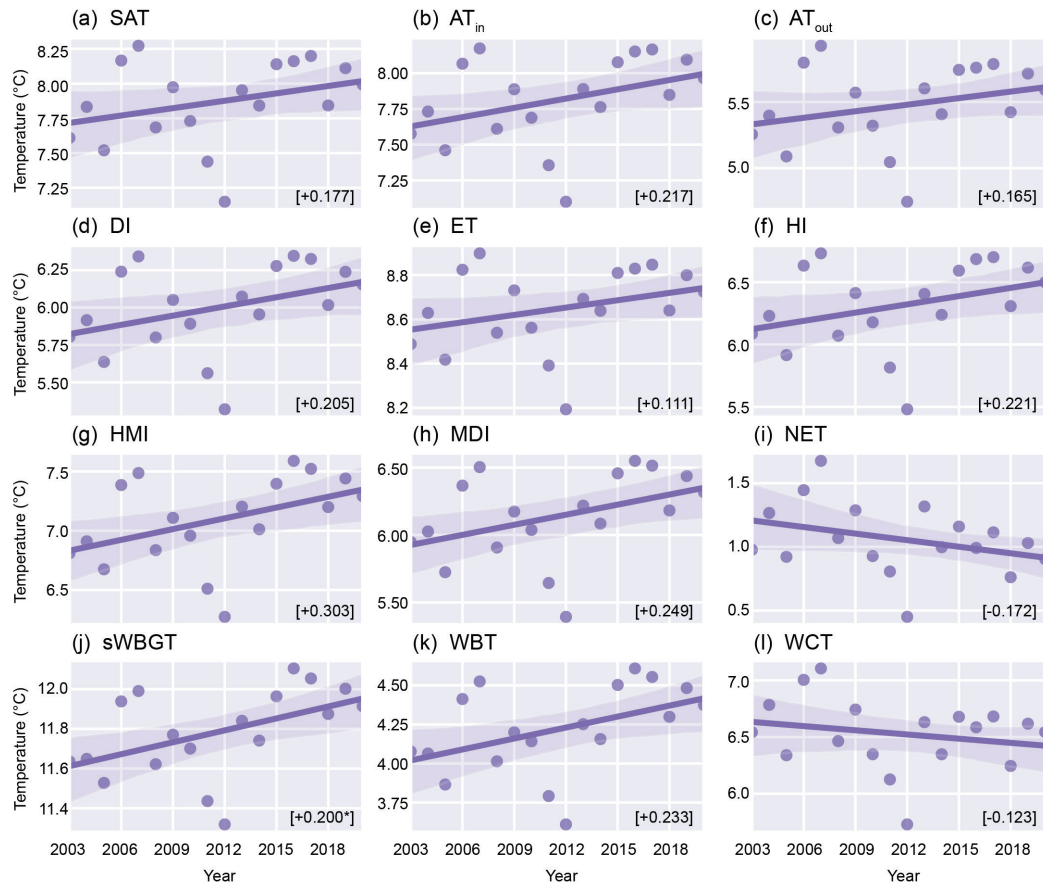
807

808

Figure 10. Spatial distributions of the 12 human thermal indices over the mainland of China in July 2020.

809

810



811

812

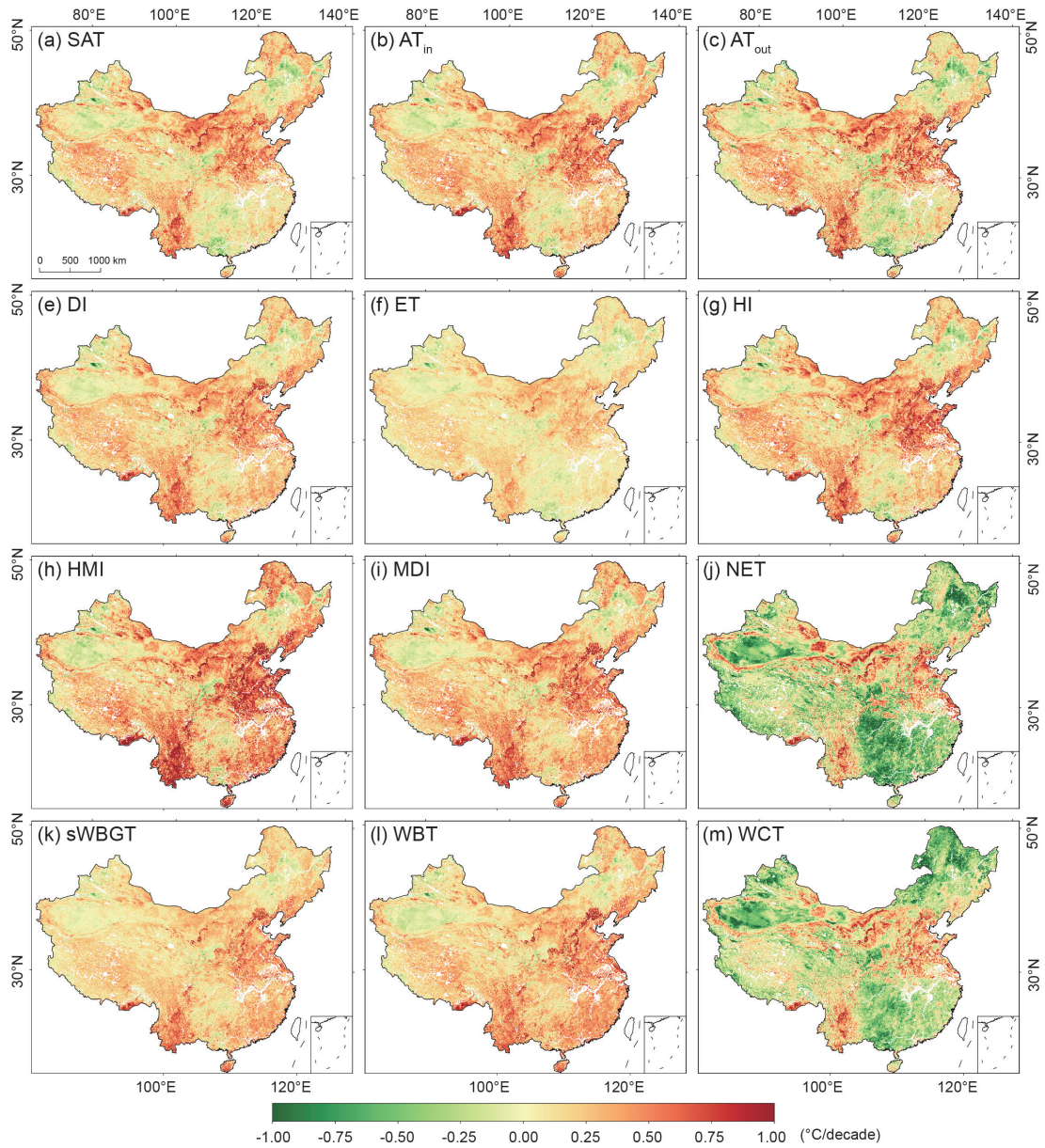
813

814

815

816

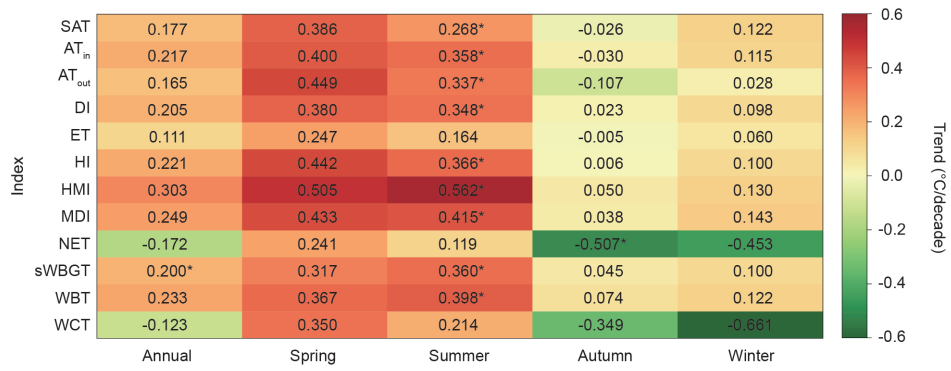
Figure 11. Temporal changes of the 12 annually-averaged human thermal indices over the mainland of China during 2003–2020. The line illustrates the linear trend, the number in the square bracket means the corresponding trend per decade, and the asterisk next to the number indicates that the trends are significant at the 0.05 level.



817

818 **Figure 12. Spatial distributions of the linear trends (unit: °C per decade) in the 12 annually-averaged human**
 819 **thermal indices over the mainland of China during 2003–2020.**

820



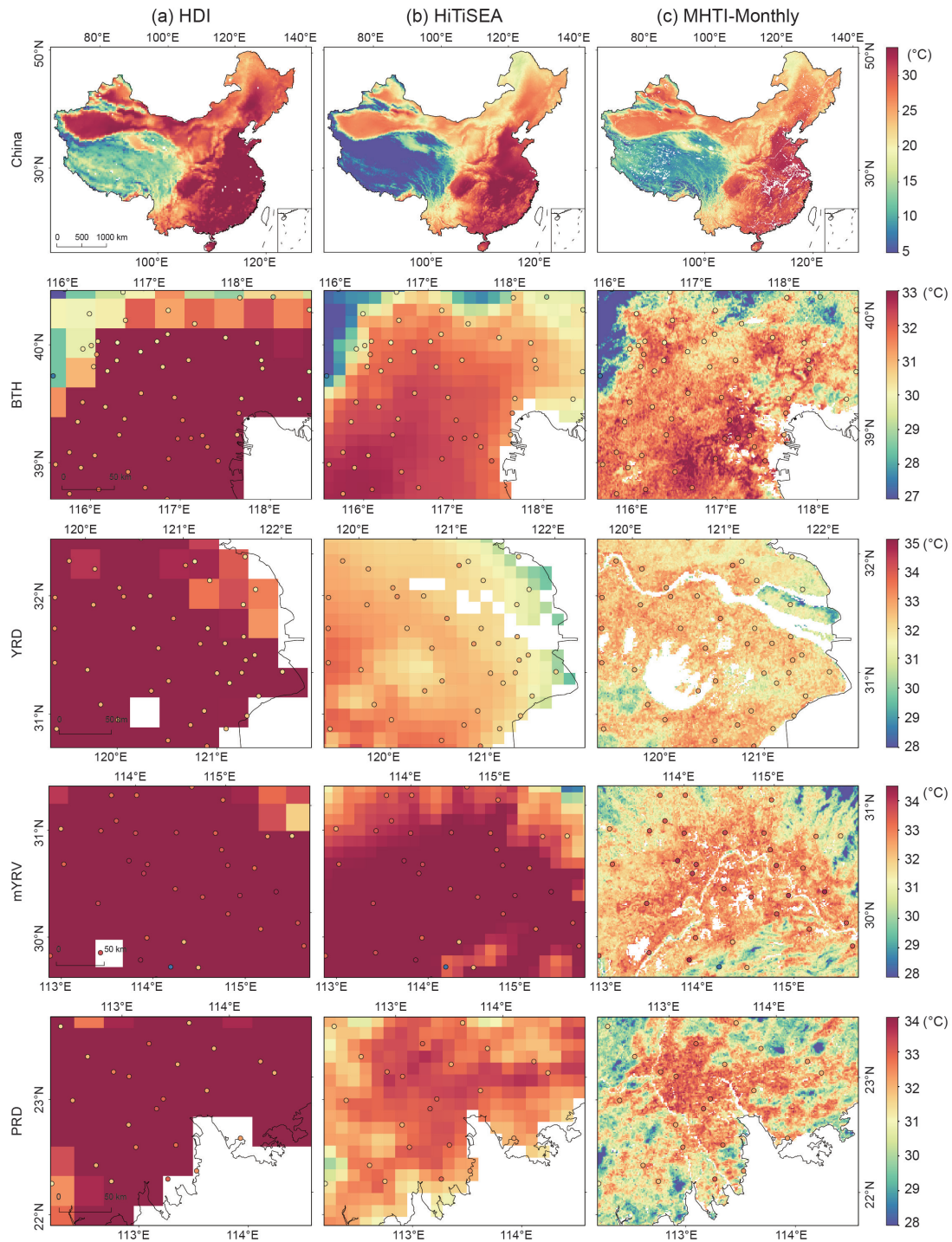
821

822

Figure 13. Temporal trends of the 12 annually- and seasonally-averaged human thermal indices over the mainland of China during 2003–2020. The number means linear trend per decade. The asterisk indicates that the trends are significant at the 0.05 level.

824

825



826

827 **Figure 14. Comparison of the spatial patterns among HDI_0p25_1970_2018 (HDI), HiTiSEA, and HiTiC-**

828 **Monthly for AT_{in} over the mainland of China and its four largest UAs in July 2018: Beijing-Tianjin-Hebei**

829 **(BTH), Yangtze River Delta (YRD), middle Yangtze River Valley (mYRV) and Pearl River Delta (PRD).**

830 **Colored circles indicate the observed AT_{in} values at individual meteorological stations.**

831

832 **Tables**833 **Table 1. Grided datasets used in this study.**

Category	Dataset	Spatial Resolution	Temporal Resolution	Variables	Data Source
Land surface temperature	A global seamless 1 km resolution daily land surface temperature dataset (2003-2020)	1 km	Daily	Land surface temperature	Zhang et al. (2022b)
Land cover	MCD12Q1.006	500 m	Annual	Land cover classes in 1 km grids	Sulla-Menashe and Friedl (2019)
Elevation	MERIT DEM: Multi-Error-Removed Improved-Terrain DEM	90 m	/	Aggregated elevation and slope in 1 km grids	Yamazaki et al. (2017)
Impervious surface	Tsinghua/FROM-GLC/GAIA/v10	30 m	Annual	Proportion of impervious surface in 1 km grids	Gong et al. (2020)
Population density	WorldPop	1 km	Annual	Population density	Gaughan et al. (2013)
Temporal variation	/	/	/	Year, Month	/

834

Table 2. Equations of the human thermal indices for each station.

Abbreviation	Human thermal index	Computation model	Reference
AT _{in}	Apparent Temperature (indoors)	$AT_{in} = -1.3 + 0.92 \times SAT + 2.2 \times E_a$	Steadman (1979)
AT _{out}	Apparent Temperature (outdoors, in the shade)	$AT_{out} = -2.7 + 1.04 \times SAT + 2 \times E_a - 0.65 \times V$	Steadman (1984)
DI	Discomfort Index	$DI = 0.5 \times WBT + 0.5 \times SAT$	Sohar et al. (1963)
ET	Effective Temperature	$ET = SAT - 0.4 \times (SAT - 10) \times (1 - 0.001 \times RH)$	Gagge et al. (1972)
HI	Heat Index*	$HI^* = -8.784695 + 1.61139411 \times SAT - 2.338549 \times RH$ $- 0.14611605 \times SAT \times RH$ $- 1.2308094 \times 10^{-2} \times SAT^2$ $- 1.6424828 \times 10^{-2} \times RH^2$ $+ 2.211732 \times 10^{-3} \times SAT^2 \times RH$ $+ 7.2546 \times 10^{-4} \times SAT \times RH^2$ $+ 3.582 \times 10^{-6} \times SAT^2 \times RH^2$	Rothfus and Headquarters (1990)
HMI	Humidex	$HMI = SAT + 0.5555 \times (0.1 \times E_a - 10)$	Masterton et al. (1979)
MDI	Modified discomfort index	$MDI = 0.75 \times WBT + 0.38 \times SAT$	Moran et al. (1998)
NET	Net Effective Temperature	$NET = 37 - \frac{37 - SAT}{0.68 - 0.0014 \times RH + \frac{1}{1.76 + 1.4 \times V^{0.75}}}$ $- 0.29 \times SAT \times (1 - 0.01 \times RH)$	Houghton and Yaglou (1923)
sWBGT	simplified Wet Bulb Globe Temperature	$sWBGT = 0.567 \times SAT + 0.0393 \times E_a + 3.94$	Gagge and Nishi (1976)
WBT	Wet-bulb Temperature	$WBT = SAT \times atan(0.151977 \times (RH + 8.313659)^{0.5})$ $+ atan(T + RH) - atan(RH - 1.676331)$ $+ 0.00391838 \times RH^{1.5}$ $\times atan(0.02301 \times RH) - 4.686035$	Stull (2011)
WCT	Wind Chill Temperature	$WCT = 13.12 + 0.6215 \times SAT - 11.37 \times (V \times 3.6)^{0.16}$ $+ 0.3965 \times SAT \times (V \times 3.6)^{0.16}$	Osczevski and Bluestein (2005)

836 SAT is observed air temperature (°C), RH is relative humidity (%), V is wind speed (m/s), and E_a is
837 actual water vapor pressure (kPa). Asterisk means that an adjustment is needed. All units of human
838 thermal indices in this study are in degrees Celsius (°C).

839

840
841

Table 3. Overall prediction accuracies of the 12 human thermal indices over the mainland of China during 2003–2020.

Indices	R^2	$RMSE$ (°C)	MAE (°C)	$Bias$ (°C)
SAT	0.9969	0.603	0.451	-0.001
AT _{in}	0.9971	0.635	0.478	0.002
AT _{out}	0.9969	0.724	0.544	0.000
DI	0.9971	0.579	0.429	0.002
ET	0.9970	0.377	0.281	0.001
HI	0.9966	0.733	0.541	0.002
HMI	0.9968	0.859	0.645	0.000
MDI	0.9969	0.664	0.493	0.002
NET	0.9949	0.856	0.620	0.001
sWBGT	0.9967	0.535	0.401	-0.001
WBT	0.9964	0.629	0.469	0.000
WCT	0.9959	0.807	0.579	0.002

842

Table 4. Comparisons of the four thermal index datasets.

	ERA5-HEAT	HDI	HiTiSEA	HiTiC- Monthly
Spatial Resolution	0.25°×0.25°	0.25°×0.25°	0.1°×0.1°	1 km×1 km
Temporal Resolution	Hourly	Daily	Daily	Monthly
Spatial Coverage	Global	Global	South and East Asia	Mainland of China
Period	1979–present	1970–2018	1981–2019	2003–2020
Thermal Indices	Mean Radiant Temperature (MRT), Universal Thermal Climate Index (UTCI)	Apparent Temperature indoors (ATind), two variants of Apparent Temperature outdoors in shade (ATot), Heat Index (HI), Humidex (HDEX), Wet Bulb Temperature (WBT), two variants of Wet Bulb Globe Temperature (WBGT), Thom Discomfort Index (DI), Windchill Temperature (WCT)	UTCI, indoor UTCI, outdoor shaded UTCI, MRT, Environment Stress Index (ESI), HI, Humidex, WBGT, WBT, WCT, AT,	SAT, AT _{in} , AT _{out} , DI, ET, HI, HMI, MDI, NET, sWBGT, WBT, WCT